Modeling Slope Microclimates in the Mars Planetary Climate Model

L. Lange, F. Forget, E. Dupont, R. Vandemeulebrouck, A. Spiga, E. Millour,
M. Vincendon, A. Bierjon

Key Points:

- We develop a sub-grid slope parameterization to simulate slope microclimates in the Mars Planetary Climate Model
- We test and validate this parameterization against observations; and reappraise frost thicknesses on Martian slopes
- This novel model opens the way to new studies on surface-atmosphere interactions for the present and past climates of Mars

Correspondence to:

L. Lange,
lucas.lange@lmd.ipsl.fr

Modeling Slope Microclimates in the Mars Planetary Climate Model

L. Lange[1] , F. Forget[1], E. Dupont[1] , R. Vandemeulebrouck[1], A. Spiga[1] , E. Millour[1], M. Vincendon[2], and A. Bierjon[1]

[1]Laboratoire de Météorologie Dynamique, Institut Pierre-Simon Laplace (LMD/IPSL), Centre National de la Recherche Scientifique (CNRS), École Polytechnique, École Normale Supérieure (ENS), Sorbonne Université, Paris, France, [2]Institut d'Astrophysique Spatiale, CNRS, Université Paris-Saclay, Orsay, France

Abstract A large number of surface features (e.g., frost, gullies, slope streaks, recurring slope lineae) are observed on Martian slopes. Their activity is often associated with the specific microclimates on these slopes, which have been mostly studied with one-dimensional radiative balance models to date. We develop here a parameterization to simulate these microclimates in 3D Global Climate Models. We first demonstrate that any Martian slope can be thermally represented by a poleward or equatorward slope, that is, the daily average, minimum, and maximum surface temperatures depend on the North-South component of the slope. Based on this observation, we implement here a subgrid-scale parameterization to represent slope microclimates (radiative fluxes, volatile condensation, ignoring slope winds for now) in the Mars Planetary Climate Model and validate it through comparisons with surface temperature measurements and frost detections on sloped terrains. With this new model, we show that slope microclimates do not have a significant impact on the seasonal CO_2 and H_2O cycles on a global scale. Furthermore, short-scale slopes (i.e., less than ∼1 km in length) do not significantly impact the thermal state of the atmosphere. Ninety-one percent of the active gullies are found where our model predicts CO_2 frost, suggesting that their activity is related to processes involving CO_2 ice. However, the low thicknesses (≤tens of cm) predicted at mid-latitudes rule out mechanisms involving large amounts (∼meters) of ice. This model opens the way to new studies on surface-atmosphere interactions in present and past climates.

Plain Language Summary Martian slopes present traces of present and past activities (e.g., dust avalanches, moraines created by past glaciers). Such activities are linked to the microclimate of these slopes: a slope oriented toward the pole will be more in the shadow and therefore colder than a slope oriented toward the equator. For now, mostly 1D models have been used to determine the microclimates present on these slopes, neglecting potential 3D atmospheric effects. Here we propose a parameterization allowing us to model such microclimates in 3D Global Climate Models. We have implemented and validated this parameterization in the Mars Planetary Climate Model by comparing our model with observations and measurements of these microclimates on the slopes. Our model shows that these slope microclimates do not significantly influence the global climate of Mars. We also provide a new CO_2 ice thickness map which constrains the possible mechanisms that form gullies on Mars.

1. Introduction

Martian slopes are associated with a wide range of present-day surface processes (Diniega et al., 2021; Dundas et al., 2021). Gullies, surface features composed of an alcove, a channel, and a depositional apron similar to small terrestrial alluvial fans, are found on slopes at mid and high latitudes (Malin & Edgett, 2000). At low to mid-latitudes, dark wedge-shaped features on high-albedo steep slopes are associated with downslope mass movements of the first micrometers of the surface, and are known as Slope Streaks (Sullivan et al., 2001). Dark features called recurring slope lineae (RSL) are also found on steep slopes that have a low albedo (McEwen et al., 2011, 2014). Other mass movements reported on Martian slopes include rockfalls and small displacements of high-latitude rocks (Dundas, Mellon, et al., 2019), polar avalanches (Russell et al., 2008), and dune-slope activity (Diniega et al., 2019, 2021).

Although the origin of these features is still debated today, most of the mechanisms proposed to explain their activity are associated with the microclimates (surface/subsurface temperatures, condensation or sublimation

of volatiles, near-surface winds) found on the slopes (e.g., Diniega et al., 2021; Dundas et al., 2021). Because of the low thickness of the Martian atmosphere today, surface temperatures and near-surface environment are mostly controlled by radiative fluxes at the surface (Savijärvi & Kauhanen, 2008). These fluxes are significantly modified for a slope compared to a flat surface. For instance, pole-facing slopes receive less solar insolation and are thus significantly colder than equator-facing slopes. Therefore, ice should preferentially accumulate on these slopes, as confirmed by current frost observations (Carrozzo et al., 2009; Dundas, McEwen, et al., 2019; Lange et al., 2022; Schorghofer & Edgett, 2006; Vincendon, 2015; Vincendon, Forget, & Mustard, 2010). Consequently, sublimation-driven processes have been proposed to explain some pole-facing slope features that are consistent with the presence of CO_2 or H_2O ice (see Diniega et al. (2021), for a complete review). Similarly, for slopes reaching the warmest temperatures, that is, equator-facing slopes, thermally stress-induced flows have been proposed to explain equator-facing slope features (e.g. Schmidt et al., 2017; Tesson et al., 2020, for RSL).

Slopes also present traces of past climates of Mars. For instance, Kreslavsky and Head (2011) reported moraines interpreted as remnants of CO_2 glaciers on steep pole-facing slopes at high latitudes. These glaciers could correspond to periods of low obliquity when pole-facing slopes are cold traps that favor the condensation of the atmosphere (Kreslavsky & Head, 2005). Conversely, at higher obliquity, around the summer solstice, surface and soil temperature of poleward-facing slopes could possibly reach the melting point of water, melting near-surface ice, possibly creating Martian debris flows features observed at mid-latitudes (Costard et al., 2002).

The consequences of slope microclimates are not limited to the surface as they also influence the thermal environment of the Martian subsurface and its contents. The Gamma Ray Spectrometer (GRS, Boynton et al., 2004) onboard Mars Odyssey has revealed the presence of subsurface water ice covered by a dry layer of regolith above $\pm 55°$ latitude, and locally down to 45° (Boynton et al., 2002), which was predicted/globally reproduced by numerical models (Leighton & Murray, 1966; Mellon & Jakosky, 1995; Mellon et al., 1997, 2004; Schorghofer & Aharonson, 2005). As pole-facing slopes are colder than surrounding flat surfaces, Schorghofer and Aharonson (2005) suggested that subsurface water ice (either pore-filling or excess ice) could be stable at equatorward latitudes beneath these pole-facing slopes. Local high-resolution subsurface ice mapping indeed showed that the depth of the ice table was correlated to topographic heterogeneity (Bandfield, 2007; Piqueux et al., 2019). Aharonson and Schorghofer (2006) modeled the theoretical stability of subsurface water ice, considering the topographic heterogeneity at high resolution, by using a 1D thermal model that accounts for sloped terrains. They found that ice could be stable at latitude as close as $\pm 25°$ compared to $\pm 45°$ for former models that do not consider slopes and their particular thermal behavior. Vincendon, Mustard, et al. (2010) also suggested that the absence of CO_2 frost at low latitudes on steep south-facing slopes in the Southern hemisphere during winter could be explained by the presence of this subsurface water ice beneath these slopes. Such results have profound implications, especially as shallow water ice can be an exploitable resource for future crewed exploration (Morgan et al., 2021).

Therefore slope microclimates are necessary to understand current surface and subsurface processes, as well as past climates of Mars. These processes are generally found on steep ($\geq 20°$) slopes that have a typical length of kilometers/tens of kilometers (Kreslavsky & Head, 1999). Such short-scale topographies and associated microclimates cannot be represented in a 3D Global Circulation Model (GCM) like the Mars Planetary Climate Model (Mars PCM, formerly known as the LMD-Mars GCM, Forget et al., 1999) which has a typical resolution of 300 km in longitude and 220 km in latitude at the equator. Mesoscale models with resolutions of tens of kilometers, either on a limited area or on the whole planetary sphere, cannot be used for long-term surface-atmosphere interactions (e.g., glacier evolution following obliquity variations over thousands of years) given prohibitive computational cost.

1D radiative equilibrium models are often used to study the environment on a slope (e.g., Costard et al., 2002; Vincendon, Forget, & Mustard, 2010; Vincendon, Mustard, et al., 2010). However, in most of these models, feedback on the large-scale properties of the meteorology is neglected while some surface processes are dependent on global circulations. For instance, the formation of water frost on the surface depends on the amount of water vapor and ice precipitation which need to be resolved by a GCM. For such studies, 1D models have been paired to outputs from 3D GCM as in Vincendon, Forget, and Mustard (2010) and Williams et al. (2022).

In this context, the implementation of sub-grid scale slope microclimates in Mars GCMs is now required to better understand the present and past surface/subsurface processes that shape the Martian environment we know today. This problem is similar to the one faced by Earth climate modelers with the sub-grid scale diversity of
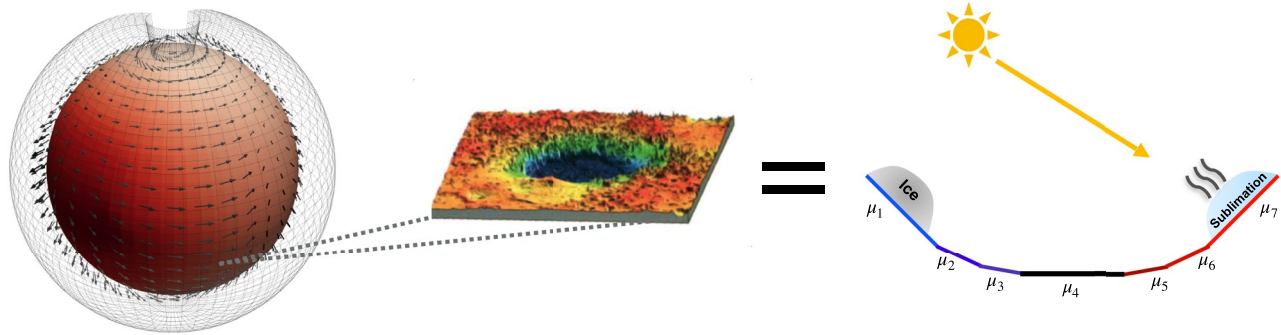
Figure 1. Schema of the sub-grid scale slope parameterization. Each coarse mesh of the global Mars PCM (left) is decomposed into sub-grid slopes (defined by characteristic slopes μ_i) (right) or flat terrain, in order to represent the slope distribution within the observed local topography (middle). These sub-grid terrains have their own microclimate (insolation, surface and sub-surface temperatures, condensation/sublimation of frosts, etc.), and the interactions between the atmosphere and surface are made through averaged values over the mesh. On the right, bluish surfaces mean colder slopes than flat surfaces (and warmer for reddish surfaces).

topography, soil, or vegetation on Earth. They use several approaches to model the interaction between the land surface heterogeneity with the overlying atmospheric layer which are known as *Land Surface Parameterization* (de Vrese et al., 2016; Flato et al., 2013; Pitman, 2003). Common approaches used, like the "mosaic" or "mixture" strategies, divides the mesh into homogeneous discrete sub-divisions where microclimates evolve. Fluxes to the atmosphere are then computed by averaging all sub-grid scale values usually weighted by their respective cover fractions, by using more complex parameterizations (Giorgi & Avissar, 1997), or set to the values computed with the sub-division that has the largest cover fractions (Dickinson et al., 1986).

We propose here to develop for Mars a similar sub-grid scale parameterization that accounts for topographic heterogeneity. The principle is illustrated in Figure 1. For each GCM mesh, we decompose the cell as a distribution of sloped terrains (defined by characteristic slopes) and a flat terrain. On each sub-grid terrain, we let the microclimates evolve so that slope-specific features (e.g., condensation of volatiles, formation of glaciers, migration of subsurface ice, etc.) can be simulated. The portion of the atmosphere above the ground within the cell sees an average of these surface microclimates, and all sub-grid terrains see the same "shared atmosphere."

In Section 2, we present the construction of the sub-grid slope representation in the model. We then describe in Section 3 the implementation of slope microclimates in the Mars PCM. An illustration of the capability of the model is given in Section 4. The validation of these sub-grid scale microclimates is presented in Section 5. Perspectives on the use of this new model are presented in Section 6, and conclusions are drawn in Section 7.

2. Representation of Slopes in the Mars PCM Meshes

The first step for the construction of our sub-grid slope parameterization is to determine a representative parameter of the surface inhomogeneity (i.e., the distribution of slopes within a mesh). We define the projected slope μ on the meridional direction as:

$$\mu = \theta \cos(\psi) \tag{1}$$

with θ the slope angle and ψ the slope orientation. We demonstrate here that any given slope (θ, ψ) can be thermally, on average, represented by a slope with a slope angle of $|\mu|$ that is either North-facing if $\mu > 0$, or South-facing if $\mu < 0$. μ will be thus the representative parameter for our distribution. To do so, we used the one-dimensional energy balance code derived from the Mars PCM (Forget et al., 1999) and described in Vincendon, Forget, and Mustard et al. (2010) and Vincendon, Mustard, et al. (2010). In short, the 1D model computes the same physical processes as in the 3D model and runs with its local properties prescribed as inputs (slope angle, orientation, optical dept of the aerosols, etc.). The effects of large-scale meteorology or slope winds are not modeled in this 1D model. The 1D model uses the method described in Spiga and Forget (2008) to compute the radiative budget on slopes, taking into account scattering by aerosols and the thermal emission from adjacent flat surfaces. We ran the model for several slope angles and azimuths on several locations on Mars, using a nominal dust opacity profile derived by averaging the available observations of dust from Martian Year (MY) 24, 25, 26, 28, 29, 30, and 31 outside the global dust storm period (Montabone et al., 2015) which is referred to as *clim dust scenario* in the
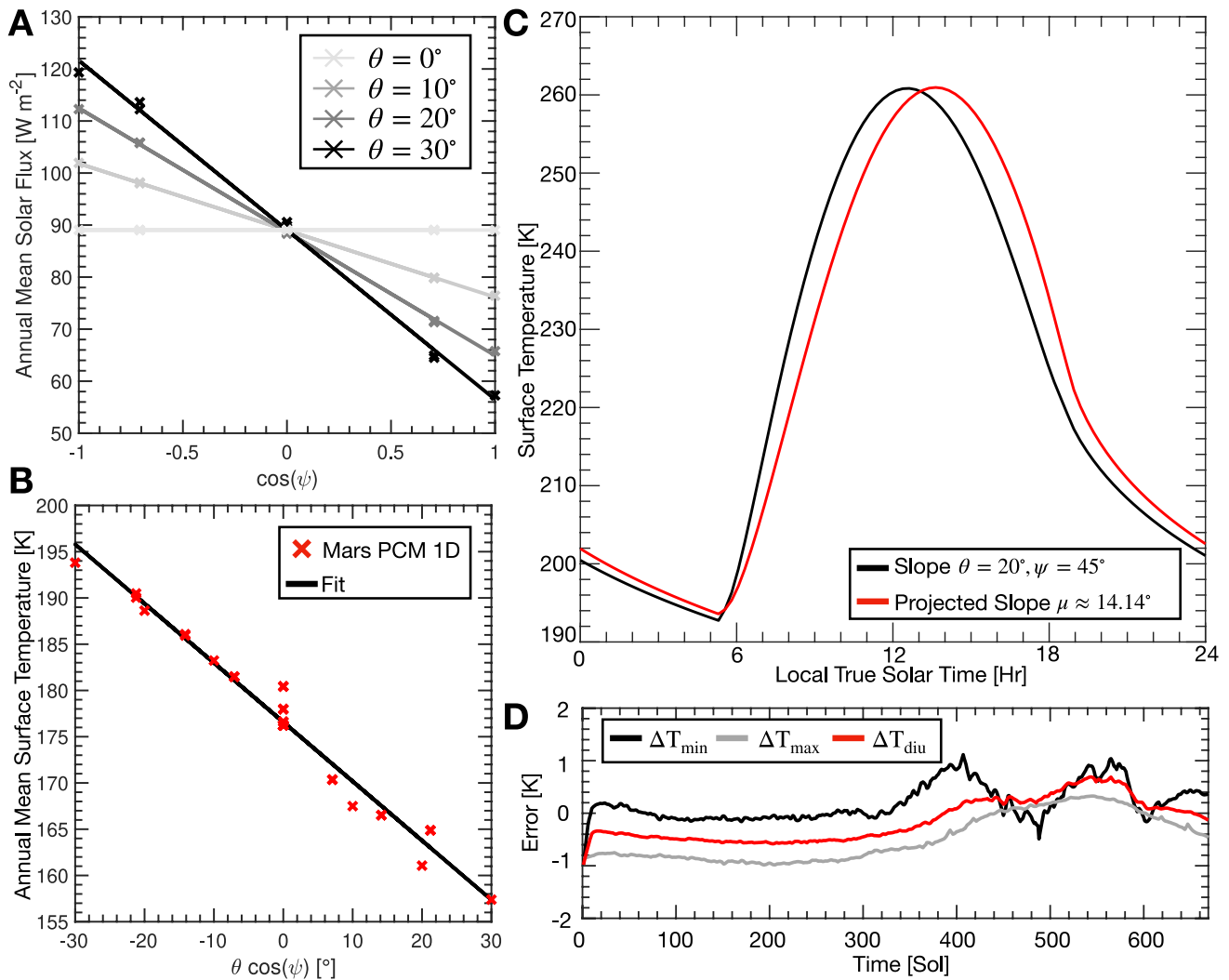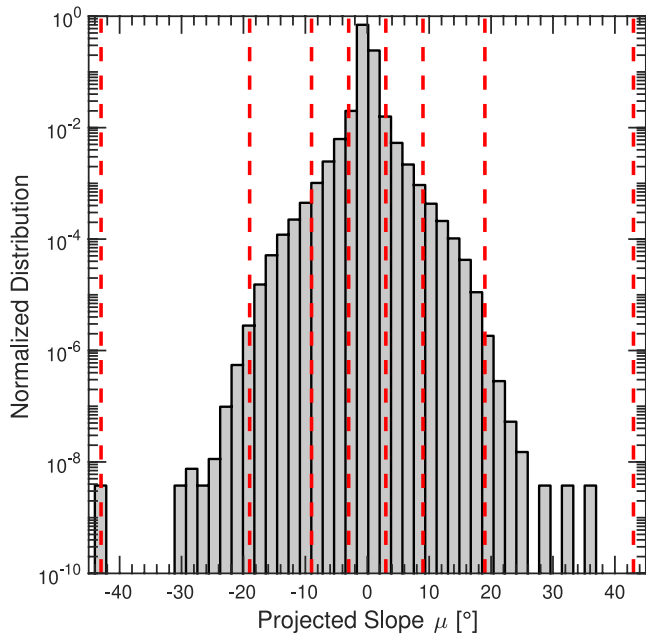
Figure 2. (a) Annual mean solar flux for several slope angles θ and azimuths ψ ($\psi = 0°$ corresponding to a slope oriented Northward) at a latitude of 70°N. Crosses represent the outputs of the 1D Mars PCM, and the solid lines are the linear interpolation connecting these points. Similar results are found at lower latitudes. (b) Correlation between the mean annual surface temperature and the projected slope μ. (c) Diurnal evolution of the surface temperature for a slope with parameters $\theta = 20°$, $\psi = 45°$ (dark); and the corresponding projected slope $\mu \approx 14.14°$ (red). The latitude is 30°N. (d) Evolution of the error ΔT obtained during a Martian year between the minimum (black), maximum (gray), and daily-averaged (red) surface temperature of the slope $\theta = 20°$, $\psi = 45°$ and the corresponding projected slope $\mu \approx 14.14°$. Similar results are found at other latitudes and with different slopes.

rest of the manuscript. Figure 2a illustrates satisfying linear correlations ($R^2 > 0.95$ in all cases) found between the parameter μ and the annual mean solar flux defined as the sum of the solar flux at infrared and visible wavelengths calculated by the model. Equivalent conclusions can be drawn using other simulations made at different latitudes. Similarly, a linear relationship ($R^2 > 0.97$) can be found between the projected slope and the surface temperature (Figure 2b). This linear relationship illustrates the fact that for any given slope (θ, ψ), the radiative energy budget can be, on average, represented by a slope with a slope angle of $|\mu|$ that is either North-facing if $\mu > 0$, or South-facing if $\mu < 0$.

We test this assumption by computing several surface temperatures for a given slope (θ, ψ) and the corresponding North/South-facing slope with a slope angle $|\mu|$ at different latitudes. An illustration is given in Figure 2c for a diurnal cycle and confirms that the North/South slope emulator has the same thermal behavior as the initial slope (θ, ψ). The difference between the two surface temperatures is caused by the difference in the slope's azimuths, which create a phase shift that evolves during the sol and the position of the sun in the sky. Apart from this phase shift, the minimum, maximum, and daily mean surface temperatures are consistent (relative error lower

Figure 3. Distribution of the projected slopes μ computed with MOLA 1/64° data set. The distribution has been normalized by dividing each count per pixel by the total number of pixels ($\sim 3 \times 10^8$). Red dashed lines represent the boundaries of the slope classes (see Table 1 for definitions).

than 1%) throughout the year (Figure 2d). The instantaneous error, created by the time lag between the two temperatures, barely exceeds 5% of the instantaneous surface temperature and is neglected. Therefore, this confirms that any sub-grid scale slopes in the Mars PCM can be either represented by pole-facing slopes or equator-facing slopes when one wishes to study the behavior of ice or any process sensitive to the diurnal or seasonal variation of surface and subsurface temperatures. Yet, our model might be limited when studying processes on East/West slopes due to the time lag between the North/South slope and the initial slope (θ, ψ). One other approach used by Williams et al. (2008) is to consider an equivalent latitude and an adjusted longitude computed from θ, ψ to correct this time shift. However, this approach was more difficult to implement in the current Mars PCM without increasing significantly the computation time as it requires recomputing the radiative transfer at each equivalent latitude and an adjusted longitude. Thus, this approach has not been adopted for our parameterization. Furthermore, in this 1D experiment, we do not consider the possible heterogeneity of albedo, thermal inertia, or the possible influence of slope winds. These effects are discussed later in Sections 3.4.3 and 3.4.5.

We then need to find how to discretize the north-south projected slopes μ to decompose our mesh into a limited subset of representative sub-grid scale slopes (Figure 1). To do so, we studied the distribution of μ computed with the Mars Orbiter Laser Altimeter (MOLA, D. E. Smith et al., 2001) data that have been widely used to study the Martian topography and slope distribution (e.g., Aharonson et al., 2003; Kreslavsky & Head, 2000; D. E. Smith et al., 2001). We used the 1/64° data set corresponding to a resolution of nearly ~ 1 km at the equator which corresponds to the typical length of key geomorphological features observed at the surface of Mars (e.g., Head & Marchant, 2003; S. Hobbs et al., 2013; Kreslavsky & Head, 2011). Note that the MOLA resolution used depends on the user's desired resolution for the sub-grid surface, and that lower or higher resolutions can be used. The MOLA data used are in a simple cylindrical format, and we have not corrected them for Mars' non-sphericity, assuming it has only a minor effect. Given the two-dimensional topographical field $h(x, y)$ where x and y are the distance in meters respectively in the longitude and the latitude direction, and h the altitude in meters at coordinates (x, y), the slope angle θ and the slope orientation ψ can be computed with Equations 2 and 3 (Spiga & Forget, 2008):

$$\tan \theta = \sqrt{\left(\frac{\partial h}{\partial x}\right)^2 + \left(\frac{\partial h}{\partial y}\right)^2} \tag{2}$$

$$\tan \psi = \frac{\partial_y h}{\partial_x h} \tag{3}$$

where $\partial_y h = \frac{\partial h}{\partial y}$, $\partial_x h = \frac{\partial h}{\partial x}$. Derivatives are calculated using centered differences with neighboring pixels. The projected slope $\mu = \theta \cos(\psi)$ is then computed. The distribution of μ is presented in Figure 3. A complete analysis of the Martian slope distribution is out of the scope of this paper, but the results obtained here (predominance of flat surfaces on Mars, the limited number of steep slopes, etc.) are consistent with dedicated studies using the same data set and similar resolution (Kreslavsky & Head, 1999, 2000). The distribution of slopes obtained is sensitive to the resolution of the MOLA data set used. As noted in Aharonson and Schorghofer (2006), a high-resolution topographic data set promotes steep slopes at the expanse of flat surfaces. Yet, at a resolution of hundreds of meters, their results (see their Figure 6) are consistent with ours, that is, flat surfaces predominate over slopes. At very low scales (resolution ≤10 m), where steep slopes are significant contributors, the Mars PCM physics and parameterizations are not adapted and would be in the domain of the Large-Eddy Simulations.

We then defined seven slope classes (delimited by the red lines in Figure 3 and defined in Table 1) that are representative of the projected slope distribution. Each mesh of the Mars PCM is divided into 7 sub-grid scale slopes that are either north-facing or south-facing, defined by a characteristic μ presented in Table 1. We assume that this

Table 1
Description of the Under-Mesh Slope Parameterization With the Slope Classes, Their Definition, and the Characteristic Projected Slope μ Associated

Class	Definition	Characteristic μ
1	$-43° \leq \mu \leq -19°$	$\mu_1 = -30°$
2	$-19° \leq \mu \leq -9°$	$\mu_2 = -14°$
3	$-9° \leq \mu \leq -3°$	$\mu_3 = -6°$
4	$-3° \leq \mu \leq 3°$	$\mu_4 = 0°$
5	$3° \leq \mu \leq 9°$	$\mu_5 = 6°$
6	$9° \leq \mu \leq 19°$	$\mu_6 = 14°$
7	$19° \leq \mu \leq 43°$	$\mu_7 = 30°$

partition with seven sub-grid surfaces (1 for the flat one, and 6 for the slopes) allows us to represent the distribution of slopes within the meshes. We could have added more classes for the decomposition but this would have increased the computation time too much without much scientific gain. Also, we cannot decrease the number of classes too much because we would lose a realistic representation of the distribution within the mesh (i.e., we would have a flat terrain and only extreme slopes). The characteristic μ proposed in Table 1 are computed as the means of the endpoints of the slope classes (except for the class 1 and 7 where it is set to 30°), rather than an average of μ weighted by the distribution within the class. The typical slope used to represent a class is exaggerated (by ~1° for classes 3–5; ~3° for classes 2–6 for instance, ~5° for classes 1–7). This choice was motivated by future studies which required modeling steep (≥25°) slopes (see for instance Sections 5 and 6).

For each mesh of the Mars PCM and each characteristic slope μ_i, we can compute the percentage of the area of the cell occupied by slopes that are in a class i (this percentage is noted δ_i hereinafter and called *cover fraction*). In this computation, the variable size of the MOLA pixels within a Mars PCM grid because of the latitude is considered. Here, and for the rest of the manuscript (if not explicitly stated), the resolution of the Mars PCM grid was 5.625° in longitude, and 3.75° in latitude (i.e., 330 km × 220 km, a standard resolution for the PCM for which the high resolution is 60 km × 60 km, i.e., 1° × 1°). Results for class 4, that is, for quasi-flat terrains, are presented in Figure 4. The distribution of the flat sub-grid surface obtained (Figure 4) is consistent with what is presented in the literature (e.g., Figure 6 of Aharonson and Schorghofer (2006)). Most of the sloped terrains are logically found in Valles Marineris, Hellas Planitia, Elysium Planitia, and the North-South dichotomy. It should be noted that at this spatial resolution, the predominant sub-grid surface (i.e., the one with the largest cover fraction) is the flat terrain. To avoid numerical artifacts, we assume that the whole mesh is flat when the area occupied by the slopes $\mu_{1,2,3,5,6,7}$ is smaller than 0.001% of the total mesh area.

Another important quantity for our parameterization is the shape of the distribution of the sub-grid slopes within a mesh. Are the sub-grid slopes uniformly distributed or on the contrary, a sub-slope is largely predominant? We calculated for each mesh the kurtosis of the real (and not discretized as in Table 1) distribution of the sub-grid slopes computed from the MOLA data set. The kurtosis is a mathematical parameter that measures the tailed-ness of the distribution. To simplify, a high kurtosis suggests that the distribution is highly concentrated around its mean, while a low kurtosis suggests a rather uniform distribution. All the calculated kurtosis are high, even for cells where the flat sub-grid surface is less dominant. The distribution of the sub-grid slopes is very narrow and centered on the flat sub-slope. We also tested these properties with a high-resolution GCM grid (1° × 1°). In that case, for some meshes, the predominant sub-grid surface is a sloped one (e.g., in Valles Marineris), and
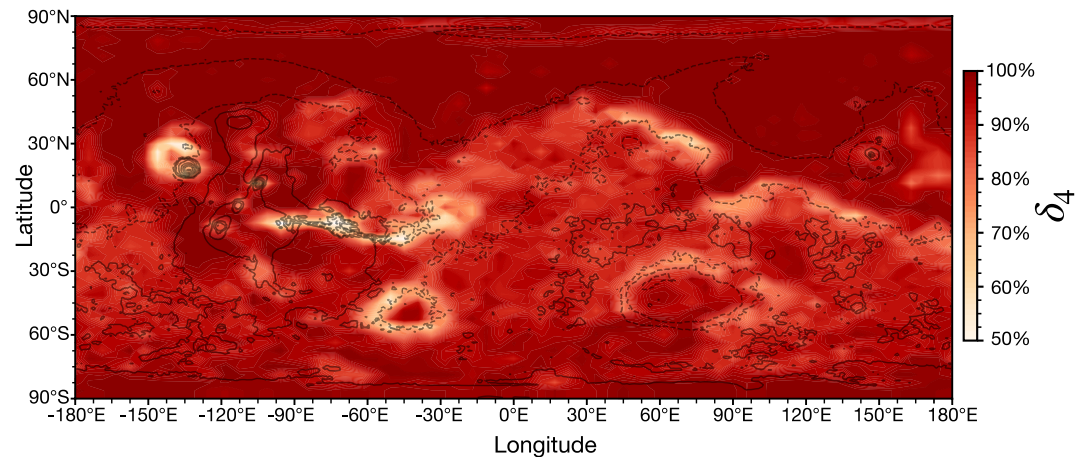
Figure 4. Cover fraction of the PCM meshes for projected slopes μ_4 (δ_4). The redder the cell, the flatter the terrains in the mesh. Black dashed lines are MOLA topographic contours.

the distribution is still tight and centered on this slope. Only 1% of the GCM grid does not have a clear peak in the sub-grid slope distribution. The consequences of the properties of the distribution are discussed in the next section.

3. Sub-Grid Scale Microclimates Modeling

We propose the following parameterization to simulate slope microclimates, inspired by the "mosaic" and "mixture" strategies in Earth models (de Vrese et al., 2016). On each binned slope, we calculate the radiative energy budget at the mesh center. Section 2 showed us that, at the given spatial resolution, the flat sub-grid surface strongly dominates. One can view the Martian topography within a mesh as a predominantly flat terrain with some sporadic slopes (where a significant amount of volatiles can condense, however). Turbulent exchanges mostly take place with the flat terrain, the slopes making only negligible contributions to the mixing. We thus assume that turbulent exchanges are solved with the predominant sub-grid surface. We compute and let evolve independently on each sub-grid slope the surface and subsurface temperatures, the volatile budget, and ground properties. We assume that these sub-grid slopes are independent and share the same atmosphere. The atmosphere only sees an averaged value of these surface fields, weighted by their cover fraction. The implementation of this strategy is detailed in Figure 5.

3.1. Energy Budget on a Slope

The evolution of the surface temperature is computed based on the energy budget at the surface:

$$\rho c_s \frac{\partial T_{\text{surf,slope}}}{\partial t} = \left(1 - A_{\text{slope}}\right) F_{\text{rad,sw}}(t) + \epsilon_{\text{slope}} F_{\text{rad,lw}}(t) + F_{\text{ground}}(t) + F_{\text{atm}}(t) + \sum_i L_i \frac{\partial m_i}{\partial t} - \epsilon_{\text{slope}} \sigma T_{\text{surf,slope}}^4(t) \quad (4)$$

where the left member of the equation is the energy of the surface layer, with ρ is the density of the ground (kg m^{-3}), c_s is the "surface layer" heat capacity per unit area (J m kg^{-1} K^{-1}) and is related to the thickness of the first soil layer (see appendix A of Hourdin (2012) and Wang et al. (2016)), $T_{\text{surf,slope}}$ the sub-grid slope temperature (K), A_{slope} (unitless) the albedo of the surface, $F_{\text{rad,sw}}$ the radiative flux at visible wavelengths (W m^{-2}), ϵ_{slope} (unitless) is the surface emissivity (assumed to be equal to the absorptivity), $F_{\text{rad,lw}}$ the radiative flux at infrared wavelengths (W m^{-2}), F_{ground} the soil heat flux due to heat conduction process (W m^{-2}), F_{atm} the sensible heat flux, $\sum_i L_i \frac{\partial m_i}{\partial t}$ the latent heat flux due to the condensation/sublimation of a volatile with a latent heat L_i (J kg^{-1}) and $\epsilon_{\text{slope}} \sigma T_{\text{surf,slope}}^4$ the radiative cooling of the surface with $\sigma = 5.67 \times 10^{-8}$ W m^{-2} K^{-4} the Stefan-Boltzmann constant. We describe below the computation of each term.

The resolution of Equation 4 is made using an implicit scheme and the soil heat conduction is solved using a finite volume approach to the problem. Surface temperature is technically linked to atmospheric and ground processes which are coupled. Following the strategy of Hourdin (2012) and Hourdin et al. (1995), the resolution is made as follows: the internal energy of the surface layer, and thus the surface temperature, is updated at time t using Equation 4. Temperatures of the subsurface layers are then updated by solving the thermal conduction. Once these temperatures are computed, the soil heat flux is computed and given as an input of Equation 4 for the next time step.

3.1.1. Radiative Fluxes

The computation of radiative fluxes accounts for CO$_2$ gas infrared absorption/emission (Dufresne et al., 2005; Forget et al., 1999; Hourdin, 1992), dust absorption, emission, and diffusion in the visible and infrared (Forget, 1998; Forget et al., 1999; Madeleine et al., 2011), and the radiative effect of water ice clouds (Madeleine et al., 2012). Dust opacity is set based on the maps from Montabone et al. (2015) and we used in the following the *clim dust scenario*.

The total irradiance computed with the current method must be adapted when considering a sloped terrain. $F_{\text{rad,sw}}$, which accounts for direct incoming flux from the sun, scattered flux by dust in the atmosphere, and the reflected flux from the neighboring terrains, is computed with the parameterization from Spiga and Forget (2008) with a slope angle $|\mu|$ and azimuth of 0° if $\mu \geq 0°$ (180° else) as inputs. For thermal infrared radiation, we assume that the atmospheric thermal radiation is isotropic and we note $F_{\text{IR,flat}}$ (W m^{-2}) the atmospheric incident thermal infrared flux on a horizontal surface computed by the PCM. Here, for a given sub-grid slope, we assume that the rest of
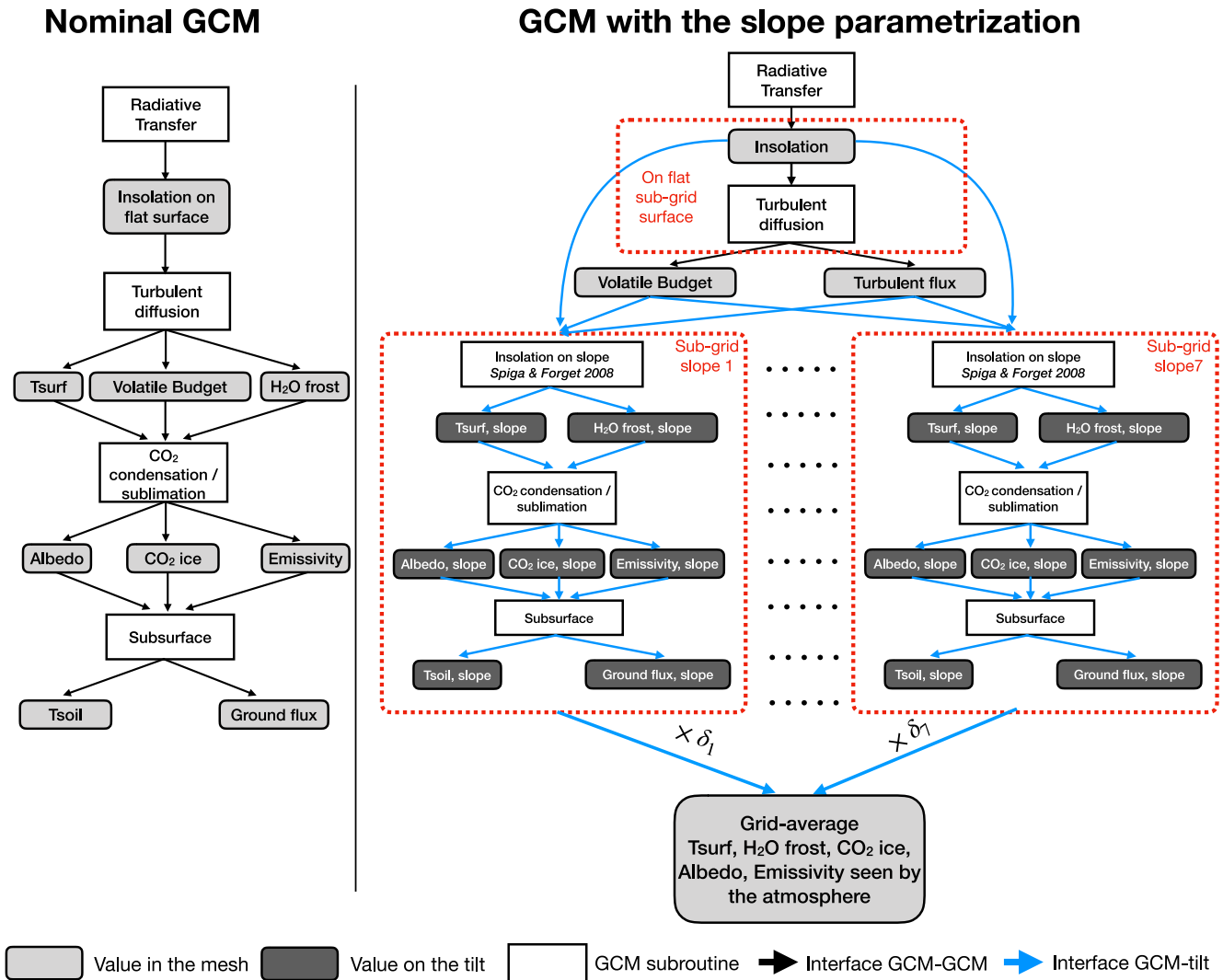
Figure 5. Description of the implementation of the sub-grid scale slope microclimates in the Mars PCM. The left part presents the architecture of the Mars PCM without the contribution of the sub-grid slopes while the right part presents the new architecture of the model, with the parameterization. Processes that only involved the atmosphere and not the surface in the Mars PCM have not been represented in the figure to clarify the diagram. T_{surf} corresponds to the surface temperature while T_{soil} refers to the subsurface soil temperature.

the mesh is flat to be consistent with Spiga and Forget (2008). The sky-view factor σ_s (unitless), which quantifies the proportion of the sky in the half hemisphere seen by the slope that is not obstructed by the surrounding terrain, is defined as in Spiga and Forget (2008):

$$\sigma_s = \frac{1 + \cos(|\mu|)}{2} \qquad (5)$$

where $|\mu|$ refer to the absolute value of the projected slope μ.

Based on geometrical considerations, the thermal infrared radiation for a sloped surface $F_{IR,slope}$ can be written as

$$F_{rad,lw} = \sigma_s F_{rad,lw,flat} + (1 - \sigma_s)\epsilon_{flat}\sigma T^4_{surf,flat} \qquad (6)$$

where ϵ_{flat} (unitless) is the emissivity sub-grid flat terrain, $T_{surf,flat}$ (K) its temperature. Here, we neglect the possible influence of the atmosphere (both in terms of absorption and diffusion) on the emission from the flat surface.

3.1.2. Sensible and Latent Heat Flux

The sensible heat flux describes the energy exchange between the atmosphere and surface due to molecular conduction and turbulence. Such flux can be written as (Forget et al., 1999):

$$F_{atm} = \rho C_H U c_{air}(T_{atm,1} - T_{surf}) \tag{7}$$

where U (m s^{-1}) is the wind velocity obtained by combining the large-scale (synoptic) wind near the surface with a gustiness wind induced by buoyancy (Colaïtis et al., 2013), c_{air} (J kg^{-1} K^{-1}) is the air specific heat capacity at constant pressure, $T_{atm,1}$ (K) the temperature of the atmosphere in the first vertical layer z_1 of the GCM (about 4 m above the surface) and C_H (unitless) is a heat transfer coefficient given by (Colaïtis et al., 2013):

$$C_H = f_h(Ri)\left(\frac{\kappa^2}{\ln\frac{z_1}{z_0}\ln\frac{z_1}{z_{0T}}}\right) \tag{8}$$

where $f_h(Ri)$ is a function of the Richardson number Ri, κ (unitless) is the von Karma constant set to 0.4; z_0 (m) is the aerodynamic roughness coefficient extracted from Hébrard et al. (2012), z_{0T} (m) the thermal roughness length. The computations of $f_h(Ri)$ and z_{0T} are detailed in Colaïtis et al. (2013). U and $T_{atm,1}$ are computed when considering the predominant sub-grid terrain.

For each sub-grid surface, water ice deposition and sublimation are computed following Navarro et al. (2014):

$$\frac{\partial m_w}{\partial t} = \rho C_H U(q_w - q_{sat}(T_{surf})) \tag{9}$$

where m_w (kg m^{-2}) is the mass of H$_2$O frost, normalized by unit area, q_w is the mass mixing ratio of water vapor in the first layer, q_{sat} is the saturation mass mixing ratio at the surface temperature (see Equation 1 of Pál et al. (2019)). The latent heat flux is then computed by multiplying by $\frac{\partial m_w}{\partial t}$ with the latent heat of sublimation of water at T_{surf}, computed from a second-order polynomial fit of Feistel and Wagner (2007)'s data.

In the model, convection near the surface promotes water sublimation through the gustiness wind induced by buoyancy (Colaïtis et al., 2013) and the stability function f_h. However, this convection is assumed to be dry, induced by the thermal contrast between the surface and the atmosphere. We, therefore, neglect convection induced by the molecular gradient of the air linked to the presence of water near the surface (e.g., Ingersoll, 1970). This should lead to a slight overestimation of the stability of water frost on the surface. We assume that the vapor pressure of water at the surface is too low to affect the molecular weight of the air and that turbulent mixing at the surface should limit the impact of this free convection (Ivanov & Muhleman, 2000). This assumption can be questioned in the case of frost with warm temperatures close to the melting point (Schorghofer, 2020). However, the model predicts water ice with a temperature $\leq$220 K, which legitimizes our approximation. Further work is needed to include these effects in future studies, particularly in the case of ice stability at high obliquity, where melting is expected (Costard et al., 2002). This requires a reparameterization of surface fluxes and a wet convection model that are beyond the scope of the paper. Nevertheless, the effect of the water latent heat term is generally neglected on Mars as it is often reduced to $\sim$1–2 W m^{-2} today (e.g., Martínez et al., 2014; Richardson, 2002); although it can become significant at higher obliquity (Naar et al., 2021).

CO$_2$ deposition and sublimation computations and the latent heat associated are made following Forget et al. (1998). For ground condensation, as CO$_2$ is abundant in the atmosphere if the surface temperature on a sub-grid slope predicted by radiative and conductive balance T_0 (i.e., Equation 4 solved without any condensation/sublimation of CO$_2$) falls below the condensation temperature at surface pressure T_{cond} (given by the Clapeyron's law using the partial pressure of CO$_2$, James et al., 1992), the amount of CO$_2$ condensing δm (kg m^{-2}) is:

$$\delta m = \frac{\rho c_s}{L_{CO_2} + c_{air}(T_{atm,1} - T_{cond})}(T_{cond} - T_0) \tag{10}$$

where L_{CO_2} (J kg^{-1}) is the latent heat of CO$_2$. This expression is almost similar to the one of Forget et al. (1998) except we add the term $c_{air}(T_{atm,1} - T_{cond})$ which corresponds to the extra heat brought by the atmosphere when cooled to the condensation temperature T_{cond} just above the surface. Even if the temperature $T_{atm,1}$ is cooled by Equation 7 and radiative processes, in the case of a pole-facing slope, the lower atmosphere lying just above the surface can be significantly warmer than the surface so this term can be significant. Typically, $T_{atm,1}$ can be 15 K

Table 2
Values of the Different Inputs for the PCM Simulation

Input	Source	Thinnest spatial resolution	Data uncertainty	Resolution used
Map Inputs				
Topography	MOLA (D. Smith et al., 1999)	500 m	~1–3 m (Neumann et al., 2001)	1 km
Thermal Inertia	TES (Putzig et al., 2005)	3 km	8% of the thermal inertia value (Putzig et al., 2005)	PCM resolution
Albedo—bare ground	TES (Putzig et al., 2005)	3 km	0.5% of the albedo value (Putzig et al., 2005)	PCM resolution
Surface roughness	Derived from TES rock abundance (Hébrard et al., 2012)	7 km	Between 10^{-2} to 10^{-4} m (Hébrard et al., 2012)	PCM resolution

Input		Range of value observed		Value used in this study
Constant inputs				
Albedo—H_2O ice		0.25–0.6, depending on dust contamination and grain size (Langevin et al., 2005)		0.33
Albedo—CO_2 ice		0.25–0.65 (Langevin et al., 2007; Titus et al., 2001)		0.65
Emissivity—bare ground		0.75–1 (Bandfield & Smith, 2003)		0.95
Emissivity—H_2O ice		0.95–1 (Vincendon, Forget, & Mustard, 2010)		1
Emissivity—CO_2 ice		0.8–1 (Piqueux et al., 2016; Titus et al., 2001)		Computed after Forget et al. (1998)

Note. 3D field inputs are presented in the upper table, while 1D inputs are given in the lower table. TES refers to the Thermal Emission Spectrometer (Christensen et al., 2001). When needed, input maps are degraded to the PCM resolution using bilinear interpolation. Albedo refers here to broadband albedo.

higher than on frosted pole-facing slopes. As such, the extra heat brought by the atmosphere when cooled can reach nearly 2% of the latent heat. In the case of atmospheric precipitation (CO_2 snow, but also other volatile deposition), we assume a uniform deposition on the whole mesh. Once δm is known, it is injected in Equation 4 which will give, after integration, T_{surf} to be T_{cond} if there is CO_2 ice on the surface.

3.1.3. Conduction in the Soil and Subsurface Water ice

The computation of the ground flux is based on the 1D layer soil model originally described by Hourdin et al. (1993) but rewritten for a physical vertical grid (in meters). The current Mars PCM solves the conduction in the soil from 0.2 mm to 25 m, corresponding respectively to one-tenth of the minimum diurnal skin depth for a thermal inertia of 30 J m^{-2} K^{-1} s$^{-1/2}$ and the maximum annual skin depth for a thermal inertia of 2,000 J m^{-2} K^{-1} s$^{-1/2}$, range of thermal inertia observed on Mars (Mellon et al., 2000; Putzig et al., 2005). Optical properties (albedo, emissivity) of the surface are set as described in Table 2 based on the Thermal Emission Spectrometer (TES) measurements (Christensen et al., 2001). We assume that all the frost-free sub-grid surfaces have the same optical properties. Compared to the former version of Hourdin et al. (1993), the current Mars PCM enables variations in the thermal properties (volumetric specific heat, thermal conductivity) with depth so that the effect of subsurface water ice can be included in the GCM. The high and mid-latitude subsurface ice reservoirs have a significant impact on the Martian climate. Because of their high thermal inertia, they store large amounts of heat during summer and restore them during winter. It thus significantly affects the CO_2 cycle through the ice deposition/sublimation (Haberle et al., 2008) and can prevent/reduce the condensation of CO_2 on pole-facing slopes (see Vincendon, Mustard, et al. (2010) and Khuller et al. (2021), for a complete discussion on the effect of subsurface ice on slope energy budget). In the current model that does not consider sub-grid slopes, maps of the ice table are created using measurements by the Mars Odyssey Neutron Spectrometer (as part of GRS) of the abundance of hydrogen near the surface (Feldman et al., 2002, 2004) and an inversion model of the effective depth of the water ice table (Diez et al., 2008).

Few observational constraints on the ice table under a slope exist (e.g., Dundas et al., 2018; Khuller & Christensen, 2021) because of (a) the resolution of the instruments used to detect subsurface water ice (e.g., more than 500 km for the spectrometers (Saunders et al., 2004) versus subsurface ice that can be ~meter thick (Dundas et al., 2018)); (b) the paucity of high-resolution observations allowing a fine determination of the ice table on the slopes based on thermal modeling (Bandfield, 2007; Piqueux et al., 2019; Vincendon, Mustard, et al., 2010). To take into account the thermal effect of the ice table on the slopes, we must model their distribution. To do so, we used the theory proposed by Leighton and Murray (1966), Mellon et al. (2004), Schorghofer and Aharonson (2005), and Aharonson and Schorghofer (2006): subsurface ice (either massive ice or pore-filling) at a depth z is stable if:

$$\frac{\overline{p_{vap,surf}}}{T_{surf}} \geq \overline{\frac{p_{sv}(T_{soil}(z))}{T_{soil}(z)}} \tag{11}$$

where overbars indicate time averages over a complete Martian year, $p_{vap,\,surf}$ (Pa) is the water vapor pressure at the surface, p_{sv} (Pa) is the saturation water vapor pressure over water ice which is a function of the temperature (Murphy & Koop, 2005). Mellon and Jakosky (1993), Schorghofer

and Aharonson (2005), and Aharonson and Schorghofer (2006) used radiative equilibrium with fixed humidity, based on the values retrieved by the TES (M. D. Smith, 2002) and do not simulate the complete water cycle. Recent sensitivity studies have shown that subsurface water ice stability is sensitive to atmospheric conditions (Song et al., 2023) as well as the presence of surface water frost (Hagedorn et al., 2007; McKay, 2009; Williams et al., 2015). Here, with the Mars PCM, we can compute more accurately the water cycle which has been validated through TES data (Naar et al., 2021; Navarro et al., 2014) and thus the vapor density at the surface considering all of these effects. We set $p_{vap,surf}$ to the near-surface vapor pressure given by the GCM if the surface is not ice-covered, $p_{sv,surf}(T_{surf})$ if it is ice-covered. When ice is stable at depth z_{ice}, we set the thermal inertia of this layer and those below to 1,600 J m^{-2} K^{-1} s$^{-1/2}$, a mid-value between completely pore-filled ice (thermal inertia of ~1,200 W m^{-2} K^{-1}; Equation 26 of Siegler et al. (2012)) and massive pure ice (thermal inertia of ~2,050 W m^{-2} K^{-1} at 180 K; P. V. Hobbs, 1974).

As water ice enhances conduction and thus the propagation of thermal waves to depth, it attenuates shallow depth temperature fluctuations, which decreases the mean vapor density and promotes the stability of subsurface water ice. Hence, the algorithm is iterated until an equilibrium is reached for the ice table depth. With this approach, we simulate for the first time the distribution of the ice table underneath slopes but also flat surfaces with a complete GCM for the atmosphere and the (sub)surface. The results are presented in a dedicated paper (Lange, Forget, Vincendon, et al., 2023).

3.2. Interaction Between Sub-Grid Surfaces and the Atmosphere

Once the microclimates have been computed and sub-grid surface properties updated, we need to communicate this information to the atmosphere by updating the mesh values. Following Earth model conventions (de Vrese et al., 2016), grid parameters are determined by averaging all sub-grid parameter values weighted by their respective cover fractions. In practice, we assume that the grid box albedo and emissivity can be computed with:

$$X = \sum_{i=1}^{7} X_i \delta_i \tag{12}$$

where X refers to the grid parameter, X_i the sub-grid parameter of slope i, δ_i the cover fraction.

In the model, condensed volatiles at the surface (i.e., seasonal frost or perennial ice) are represented with surface mass density (kg m^{-2}). However, the area of the sloped mesh grid is not the same if it is sloped or flat, assuming a similar latitude/longitude boundary for the cell. Hence, to ensure mass conservation, condensed volatiles at the surface are computed with:

$$X = \sum_{i=1}^{7} X_i \frac{\delta_i}{\cos(\mu_i)} \tag{13}$$

where μ_i is defined in Table 1.

For surface temperature, we assume that we can average the Stefan–Boltzmann function:

$$\epsilon \sigma T_{surf,grid}^4 = \sum_{i=1}^{7} \epsilon_i \sigma T_{surf,i}^4 \delta_i \tag{14}$$

where ϵ (unitless) is the grid emissivity, $T_{surf,grid}$ (K) the grid surface temperature, and quantities with subscript i refer to the same quantities but for the sub-grid slope.

3.3. Post-Processing and Interpolation

The proposed model allows, for each grid point, to determine the surface fields for the seven types of slopes modeled here (Figure 1, Table 1). The question is now: for any point on the Martian surface, knowing the characteristics of the terrain (slope and azimuth), can we determine the values of the surface quantities (e.g., CO_2 frost, H_2O frost, surface temperature) using the GCM outputs that are discretized in space and slopes?

Let us consider a point (noted M) of the surface of Mars, placed on a surface of slope angle θ and azimuth ψ. We compute μ and find the index i, $i + 1$ of the two GCM sub-grid slopes such that:

$$\mu_i \leq \mu < \mu_{i+1} \tag{15}$$

The point M is surrounded by four GCM meshes. We can interpolate the values obtained at the GCM points for the sub-grid slope μ_i and μ_{i+1} at point M. This is performed by using a bilinear interpolation in space. After that, the value for slope μ at M is obtained with linear interpolation between the fields obtained after the bilinear interpolation for μ_i and μ_{i+1}. If $\mu < \mu_0$ or $\mu > \mu_7$, an extrapolation is computed. Thus, we have virtually access to any surface field for any kind of sloped surface on Mars using this complete climate model. We acknowledge that (a) we assume linear interpolation on processes that are not necessarily linear (although we interpolate neighboring points); (b) we neglect the time-shift (generally lower than 1–2 hr) for slopes oriented East-West (Figure 2c).

3.4. Discussions on the Modeling Assumptions

3.4.1. East-West Component of the Slope

We have demonstrated in Section 2 that our parameterization is suitable to represent the diurnal (minimum, maximum, and daily mean) and seasonal variations of the (sub)surface temperatures of any slopes through its projected slope μ. However, the parameterization is not adapted to reproduce the instantaneous (sub)surface temperature for a slope with an East-West component. As shown in Figures 2c and 2d, the time shift created by the azimuth of the slope is not reproduced when simulating the thermal behavior of the slope with the parameter μ. This will impact the comparison with surface temperature measurements (Section 5.1: the impact can be as high as ± 10–15 K) (Figure 2c).

3.4.2. Effect of Surrounding Topography

It is assumed for the computation of the reflected flux that for a given sub-grid slope, the rest of the mesh is flat. We acknowledge here that this assumption is simplifying but considering non-flat surrounding terrains would generate a much more sophisticated form factor calculation (e.g., Dozier & Frew, 1990), as well as a radiative coupling problem between all sub-grid surfaces (e.g., Section 2 of Schorghofer (2022)). Furthermore, the model neglects shadowing created by surrounding slopes. Hence, cold traps found in gully alcoves for instance (Schorghofer, 2020) are not well represented.

3.4.3. Sub-Grid Surface Thermophysical Properties

We assume that the thermophysical properties (albedo, emissivity, thermal inertia, see Table 2) of the coarse-resolution main grid apply to the sub-grid surfaces (if they are frost-free). However, surface heterogeneities have been observed at $\sim$ km scale (e.g., Ahern et al., 2021), which can lead to significant differences in the surface temperatures. For instance, an error of $\sim 100 \, \mathrm{J \, m^{-2} \, K^{-1} \, s^{-1/2}}$ on the thermal inertia can lead an error of 10 K on the surface temperature (Figure 1 of Putzig and Mellon (2007)); an error of ± 0.1 on the albedo or ± 0.05 on the emissivity would lead to an error of less than 5 K (Figure 1 of Putzig and Mellon (2007) and Bandfield and Feldman (2008)). Nevertheless, our assumption seems reasonable as no clear constraints exist for the slope surface properties: some exhibit dust/sand (e.g., Tebolt et al., 2020) while others expose bedrock/high thermal inertia material (e.g., Edwards et al., 2009).

3.4.4. Turbulent Exchanges and Common Atmosphere Between the Sub-Grid Surfaces

We assumed in the parameterization that the turbulent exchanges are done with the predominant sub-grid surface and that all sub-grid surfaces share the same atmosphere. We acknowledge here that this scientific can be discussed. For instance, Earth climate models have shown that turbulent mixing processes can be significantly different when sub-grid variability is considered (de Vrese et al., 2016; Mahrt, 2000; Molod et al., 2003). However, on Mars unlike on Earth, surface-atmosphere thermal exchanges are strongly dominated by radiative fluxes (computed for each slope) rather than turbulent sensible heat flux (Read et al., 2017).

The assumption that sub-grid surfaces share a common atmosphere column can also lead to inaccuracies, particularly in near-surface thermal environments. The near-surface atmosphere energy budget is primarily controlled by the radiative process associated with the slope over the first 500 m (i.e., reflected irradiance and atmospheric absorption). Above 500 m, the increasing thermal gradient leads to the dominance of convection for the next several kilometers (Read et al., 2017). As a result, the first few hundred meters of the atmosphere may be colder over a poleward-facing slope than over a flat area. It should be noted that even if convection is not dominant, it would also alter the near-surface environment, and help to homogenize the atmosphere (Colaïtis et al., 2013). However, building a parameterization for this convective activity for $\sim$km slope, that is, in the "gray zone" (or "Terra Incognitae" Wyngaard, 2004) for resolved/parameterized convection would require a dedicated study using Large Eddy Simulations and is out of the scope of this paper.

The infrared emission by the atmosphere comes mainly from altitudes between 2 and 10 km (Figure 2 of Dufresne et al. (2005)). The atmosphere at these altitudes is not influenced by small slopes (less than 1 km in height difference, as observed on craters for instance, e.g., Vincendon, Forget, & Mustard, 2010; Vincendon, Mustard, et al., 2010) because it is mixed by winds at altitudes that do not see this small relief. For these terrains, the approximation of a shared atmosphere for the calculation of the infrared flux is therefore valid. For more significant slopes (important differences in level or length of several tens of km, e.g., canyon), this hypothesis is more questionable in addition to the non-consideration of the slope winds which might play a major role. Furthermore, our approach assumes that the winds will effectively mix these air masses such that one can adopt a common atmospheric column for all sub-grid surfaces in the analysis. Indeed, the observed Martian slopes in our study tend to be a few kilometers wide and are separated by distances on the order of tens of kilometers. The near-surface winds have speeds of several meters per second which can mix the atmosphere between slope regions over periods of nearly tens of minutes. With our physical time-step of 15 min, we assume that this time is enough to mix the air masses and have a common atmospheric column between the sub-grid slopes.

3.4.5. Effect of Slope Winds on the Sensible and Latent Heat

Because of the low density and heat capacity of the Martian atmosphere, the sensible and latent heat terms generally lead to negligible contributions compared to the radiative fluxes in the Martian surface energy budget (Martínez et al., 2014; Savijärvi & Määttänen, 2010). However, Spiga et al. (2011) have demonstrated that during the night, katabatic winds can locally reinforce the sensible heat flux which becomes comparable to the thermal infrared cooling of the surface. Anabatic slope winds could also explain colder-than-expected surface temperatures during the afternoon (Spiga et al., 2011).

Slope winds have also an effect on the sublimation of H_2O as it is controlled by the wind velocity (Equation 9). As slope wind speeds can be ∼10 times higher than those for a flat surface, they can have great importance when modeling H_2O ice stability. Experiments using the 1D model showed that high slope winds could reduce the ice stability by tens of sols (Vincendon, Forget, & Mustard, 2010).

Subgrid-scale parameterization of slope winds deserves a dedicated study and is left as a future work on how its impact on slope microclimates can be represented in Global Climate Models.

3.4.6. Interpolation Sub-Grid Surfaces and Grix Box Average

Grid-box average (Section 3.2) or post-processing (Section 3.3) are done using (bi)linear interpolation or linear average, weighted by the cover fraction. However, such methods are applied to processes that might be non-linear. These interpolations/communications between sub-grid heterogeneity and GCM grid box have been studied and reviewed in the Earth climate community (e.g., Giorgi & Avissar, 1997) and future improvements of our parameterization should consider this point.
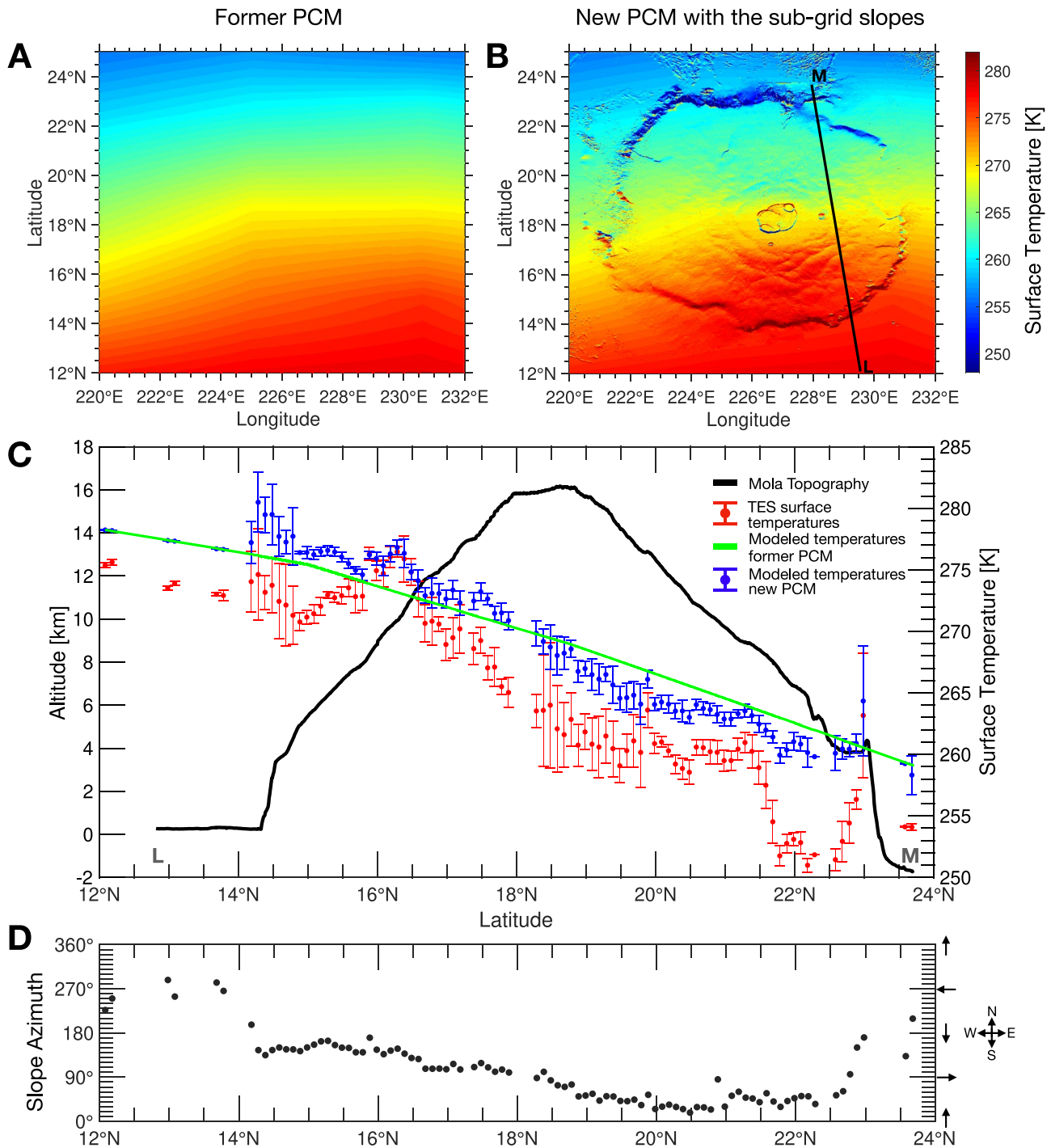
4. An Illustration in the Olympus Mons Region

Here we illustrate the improvements achieved with this sub-grid slope parameterization by giving an example in the region of Olympus Mons (12°–25°N, 220–235°E). Figure 6a illustrates the surface temperatures predicted by the PCM without the parameterization. In this version, surfaces modeled by the PCM are only flat, so no temperature variation related to topography can be detected. Figure 6b illustrates the surface temperatures predicted by the PCM with the sub-grid parameterization in this same region, after the post-processing described in Section 3.3. With this version, the obtained "thermal image" and the surface temperature distribution of the area are more realistic: surface temperatures vary with the topography and the slopes. The reliefs of Olympus Mons appear naturally because of the topographic gradients that create surface temperature differences. We recover expected observations: the flanks of Olympus Mons oriented toward the equator are warmer than those oriented toward the North. The same conclusions for the caldera of the volcanoes can be drawn. Similar observations are drawn when repeating this experiment in different regions (e.g., Valles Marineris, Tharsis, etc.). This example is used for the validation in the next section.

5. Validations of the Implementation

5.1. Validation of the Surface Temperature

We compare here the surface temperatures predicted by our model on slopes with observations on warm (daytime), intermediate (dawn/sunset), and cold (night/shadow) surfaces. To do so, we used surface temperatures

Figure 6. Surface temperatures predicted by the PCM in the Olympus Mons region at $L_s = 270°$ (L_s being the solar longitude), at 2 p.m. for (a) the PCM without the sub-grid slope parameterization (b) the PCM with the sub-grid slope parameterization. Maps have a resolution of 128 pixels per degree. No MOLA background has been added to the plot. (c) Comparison between the surface temperatures measured by Thermal Emission Spectrometer (TES) (red dots) and prediction by the former PCM (green line) and new PCM (blue dots) on transect L-M (panel b). PCM predictions and TES measurements are binned: dots represent the mean value, and the error bars represent their standard deviation (σ). (d) Azimuth of the slopes where TES measurements are made.

measured by TES and the Thermal Emission Imaging System (THEMIS, Christensen et al., 2004) infrared imager. The TES instrument includes a spectrometer in the 6–50 μm band and co-aligned visible (0.3–2.7 μm) and thermal (5.5–100 μm) bolometers providing measurements with a ∼3–8 km resolution in a ∼380 km footprint (Christensen et al., 2001). THEMIS includes a thermal bolometer in the 7–15 μm band and provides surface temperature measurements with a resolution of ∼100 m within a footprint of ∼32 km. In this study, we use TES kinetic surface temperatures derived from spectral measurements because of their low sensitivity to atmospheric effects (Bandfield & Feldman, 2008). Furthermore, the emissivity used for TES retrievals is equal to the one of the PCM. THEMIS measures spectral radiance emitted by the surface and converts it to brightness temperature assuming a surface emissivity of one and without applying atmospheric correction (Christensen et al., 2003). Therefore, to mitigate these effects, we only considered surface temperatures acquired by THEMIS after 6 p.m. and before 8 p.m., or between 6 a.m. and 8 p.m. At these local times, simulations with the PCM indicate that the temperature contrast between the atmosphere and the surface should be low, so the atmospheric correction, which is not done during THEMIS post-processing, should be negligible. Furthermore, we assume that at these times, the surface has cooled enough so that the effects of albedo variability during the day on temperatures have disappeared. We also assume that just after sunset, the effect of thermal inertia heterogeneity on slopes is not yet significant enough to introduce a bias during the comparison. For this last point, observations at 5 p.m. would have been preferable but the effect of slope azimuth on surface temperatures would still have been marked at these hours. Since these temperatures are calculated assuming an emissivity of 1 and the PCM assumes an emissivity of 0.95 we corrected these temperatures by a factor $0.95^{-1/4}$. Lastly, as THEMIS has a thin resolution, we have degraded the images to a resolution of 1 km, a resolution similar to the parameterization used in this section (MOLA file with a resolution of ∼1 km at the equator to generate the sub-grid statistics).

5.1.1. Daytime Surface Temperatures

For the daytime comparison, we looked at the Olympus Mons region, which has steep slopes and a surface with homogeneous properties. We present a comparison at L_s = 270° (Northern autumn) at 2 p.m. in Figure 6c. TES measurements presented here have been made during Martian Year 26 on the transect LM (Figure 6b). For each measurement, we retrieved the slope angle and azimuth associated and computed the predicted surface temperatures using the method presented in Section 3.2. We then binned the measurements and simulated temperatures on 0.1° latitude segments. As expected, the distribution of the surface temperatures with the parameterization is better (mean error of −4.2 ± 2.3 K at 1-σ) compared to the former PCM (mean error of −4.5 ± 3 K at 1-σ). The model performs less well (error of ∼5 K) when the slope has a strong east-west component (e.g., latitudes 16–19°N, Figure 6d). This is due to the choice of representing the slope by its meridional component, which therefore does not lead to a satisfactory simulation of the instantaneous temperature for this type of slope. Surface temperatures are overestimated (+5–10 K) by the PCM, especially on the flank of the volcano where the steepest slopes are found. This might be caused by (a) the vertical representation of dust in the PCM; (b) katabic slope winds (not represented in the model) which should cool down the atmosphere and decrease the surface temperatures (Spiga et al., 2011). The low contrast in surface temperatures predicted by the model is explained by the low slope angles found in the transect (except at the base of the volcano), and the azimuth of the terrains which reduces the values of μ ($\mu \leq$ 4–5° generally). Other surface temperature transects investigated show similar results in this region, as well as in Valles Marineris.
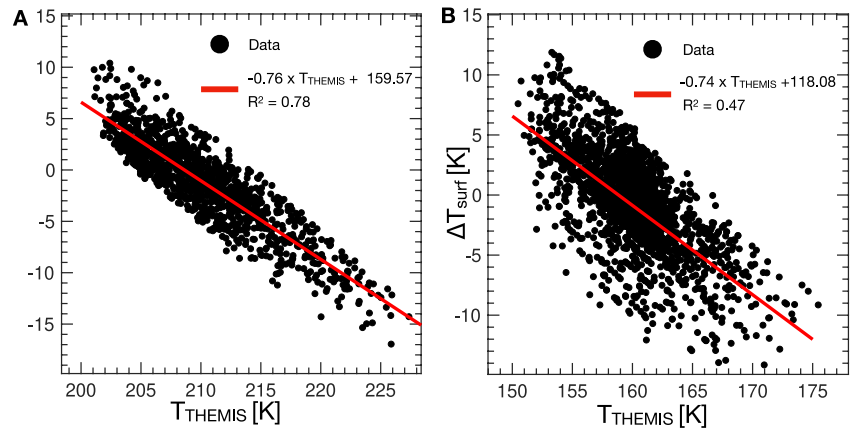
5.1.2. Sunset Surface Temperatures

We then looked at temperatures acquired at sunset, which are intermediate during the warm temperatures of the day and cold ones at dawn. An example of validation is presented in Figure 7. Here, we looked at the area at Gasa crater (35.7°S, 129.4°E) during Southern spring. In this region of interest (ROI, defined by the boundaries given in Figure 7a), the majority of the surfaces is flat, and the steep terrains are confined to the craters where significant slopes can be found (δ_4 = 85% here). THEMIS measured surface temperatures that are on average ∼210 K, mostly on flat surfaces (Figure 7a) with extreme temperatures found on East-South and West-Equatorward facing slopes (between 200 and 227 K respectively). The former PCM, without the sub-grid slope parameterization, that is, which computes surface temperature only for flat terrains, gives a mean surface of ∼209 K, in good agreement with THEMIS observations but was not able to reproduce the cold and hot temperatures found on the slopes. The new parameterization helps to reproduce a realistic field where thermal contrasts created by the topography are apparent (Figure 7b). The difference between the PCM and THEMIS surface temperatures (Figure 7c) reveals two interesting features. First, some differences exist between the PCM and the observations on flat surfaces
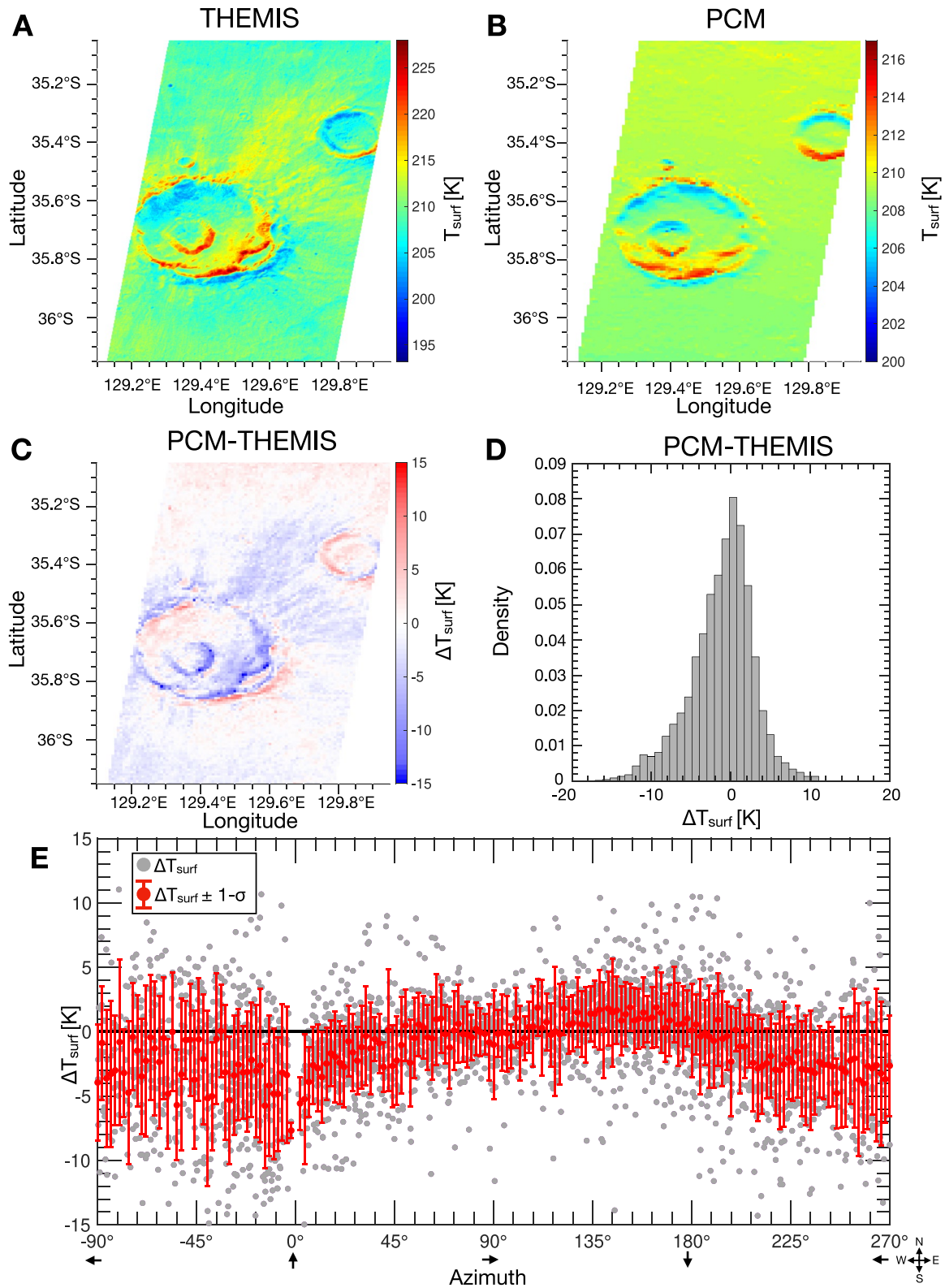
Figure 7. (a) Surface Temperature obtained by THEMIS around Gasa crater on image I89710003 (35.7°S, 129.4°E) obtained at $L_s = 181°$ and local time = 7.08 p.m. (b) Surface Temperature predicted by the PCM with the sub-grid slope parameterization. (c) Difference between the PCM and THEMIS measurements (d) Histogram of the difference between the PCM and THEMIS measurements on steep (slope angle ≥9°) slope. (e) Difference between the PCM and THEMIS measurements on slopes with a slope angle higher than 9° versus the slope's azimuth.

Figure 8. Comparison between the surface predicted by the PCM and measured by THEMIS versus the surface temperature measured by THEMIS for (a) I89710003 and (b) I63705006.

(e.g., 35.2–35.5°S, 129.4–129.6°E). These small differences are due to sub-kilometer variability in the thermal inertia that is not caught by the PCM. Second, the PCM seems to underestimate the surface temperatures on equatorward-facing slopes compared to THEMIS, whereas it overestimates it for pole-facing slopes (Figure 8a). However, Figures 7c and 7e show that the most significant differences are found on East-West slopes (Figures 7c and 7e), where the PCM can be 4 K ($\pm$4 K at 1-σ) colder for a North-East-facing slope, or 4 K ($\pm$2 K at 1-σ) warmer for a South-West facing. On the contrary, for North-South facing slopes, the differences are limited to less than 1–2 K ($\pm$2 K at 1-σ). Again, this is due to the slope parameterization, which does not model the slope's azimuth effects (Section 3.4.1). Thermal inertia effects also contribute to the difference between the observed and simulated temperatures as the slopes presented here present a higher thermal inertia ($\geq$1,000 J m^{-2} K^{-1} s$^{1/2}$) than the one used in the PCM (210 J m^{-2} K^{-1} s$^{1/2}$). Finally, this underestimation of maximum and minimum temperatures on slopes may be linked to: (a) the common atmosphere between each sub-slope: North-facing slopes have a colder near-surface atmosphere than in reality, which could lead to an underestimation of the infrared flux. This underestimation would be limited to 1 W m^{-2}, given that the radiation comes mainly from an altitude of 2–10 km (Dufresne et al., 2005), where atmospheric temperatures are homogeneous; (b) An overestimation of a scattering component for steep slopes, as the parameterization of Spiga and Forget (2008) is indeed less efficient for such slopes. Nevertheless, the comparison between the temperatures simulated by the model and observed by THEMIS on steep slopes (slope angle $\geq$9°) (Figure 7d) shows that modeled temperatures have an error of −1.3 K ($\pm$4 K at 1-σ). Other comparison made in other locations give similar results.

5.1.3. Cold Surface Temperatures at Dawn

We checked here our surface temperatures with observations acquired at dawn when the surface temperatures are the coldest. An illustration is given at 44.4°S, 111.8°E (close to Greg crater) in Figure 9. The image was acquired at 7.41 a.m. during Southern Winter. Shadowed pole-facing slopes have a surface temperature that is within 5 K of the CO_2 frost point (150 K for the typical pressure at this location), suggesting the presence of CO_2 ice (Khuller et al., 2021; Lange et al., 2022). As the emissivity of CO_2 ice varies with crystal size (Piqueux et al., 2016, and references therein), we did not apply the $0.95^{-1/4}$ correction for these areas. The observation of CO_2 frost on pole-facing slopes at such latitudes is consistent with observations from Vincendon, Mustard, et al. (2010), Khuller et al. (2021), and Lange et al. (2022). The same observations as those described previously are found here: sub-grid differences between the model and the observations that are created by sub-grid differences of thermal inertia, and the influence of the slope azimuth. When comparing the slope surface temperatures (Figures 8b and 9d), we found that the model is colder than the observations (−1.1 $\pm$ 5 K at 1-σ). The difference varies with the slope's orientation (Figure 9e), with again, pole-facing slopes being warmer and equatorward facing slopes being colder by 2–3 K ($\pm$4 K at 1-σ).

5.1.4. Generalization and Conclusion

We extend the study presented above to other regions of Mars. Similar conclusions to those presented above can be drawn. The average surface temperatures predicted by the PCM and what is observed by THEMIS are
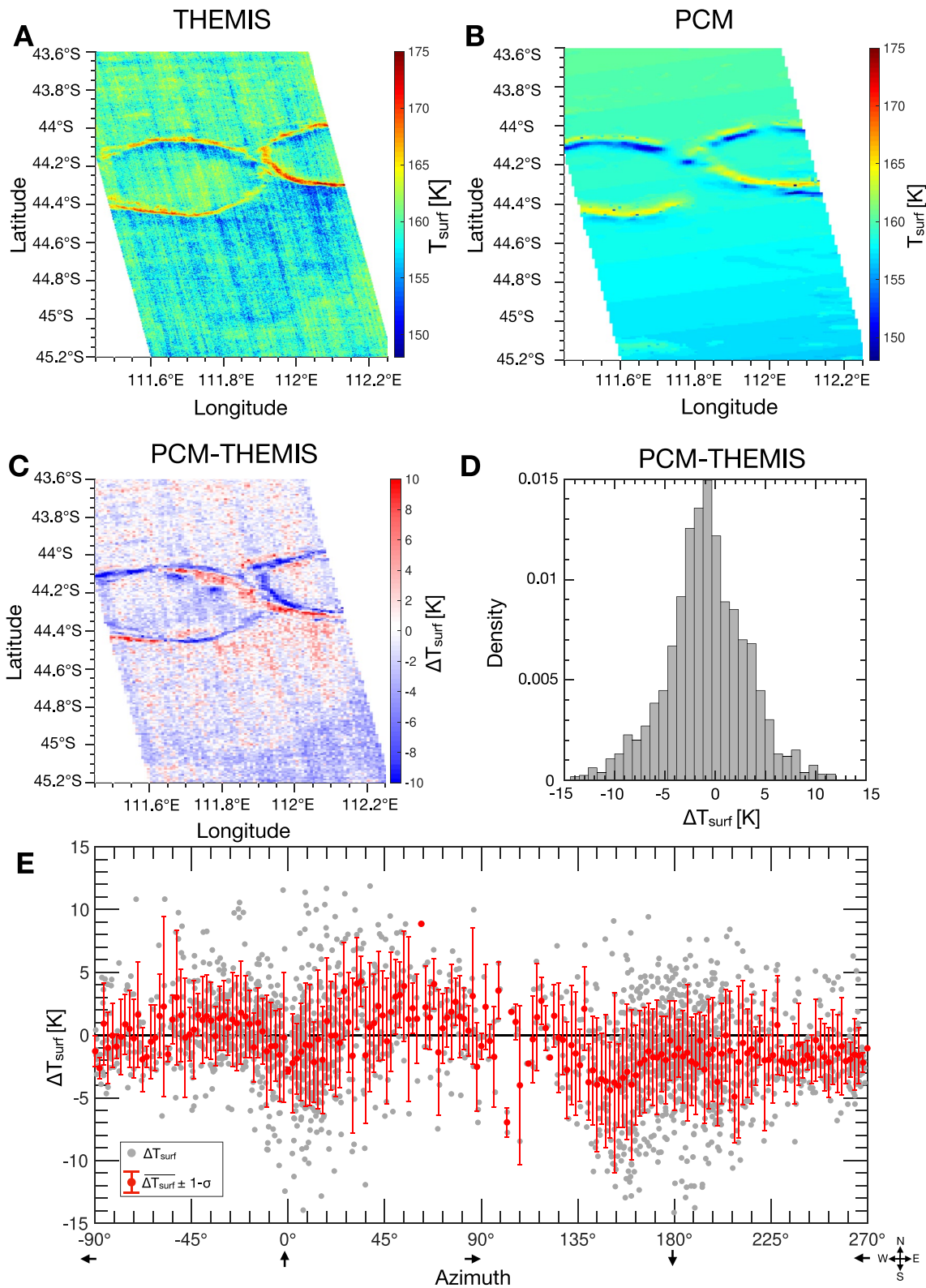
Figure 9. (a) Surface Temperature obtained by THEMIS on image I63705006 (44.4°S, 111.9°E) obtained at L_s = 142.13° and local time = 7.41 a.m. (b) Surface Temperature predicted by the PCM with the sub-grid slope parameterization. (c) Difference between the PCM and THEMIS measurements (d) Distribution of the difference between the PCM and THEMIS measurements on steep (slope angle ≥9°) slope. (e) Difference between the PCM and THEMIS measurements on slopes with a slope angle higher than 9° versus the slope's azimuth.
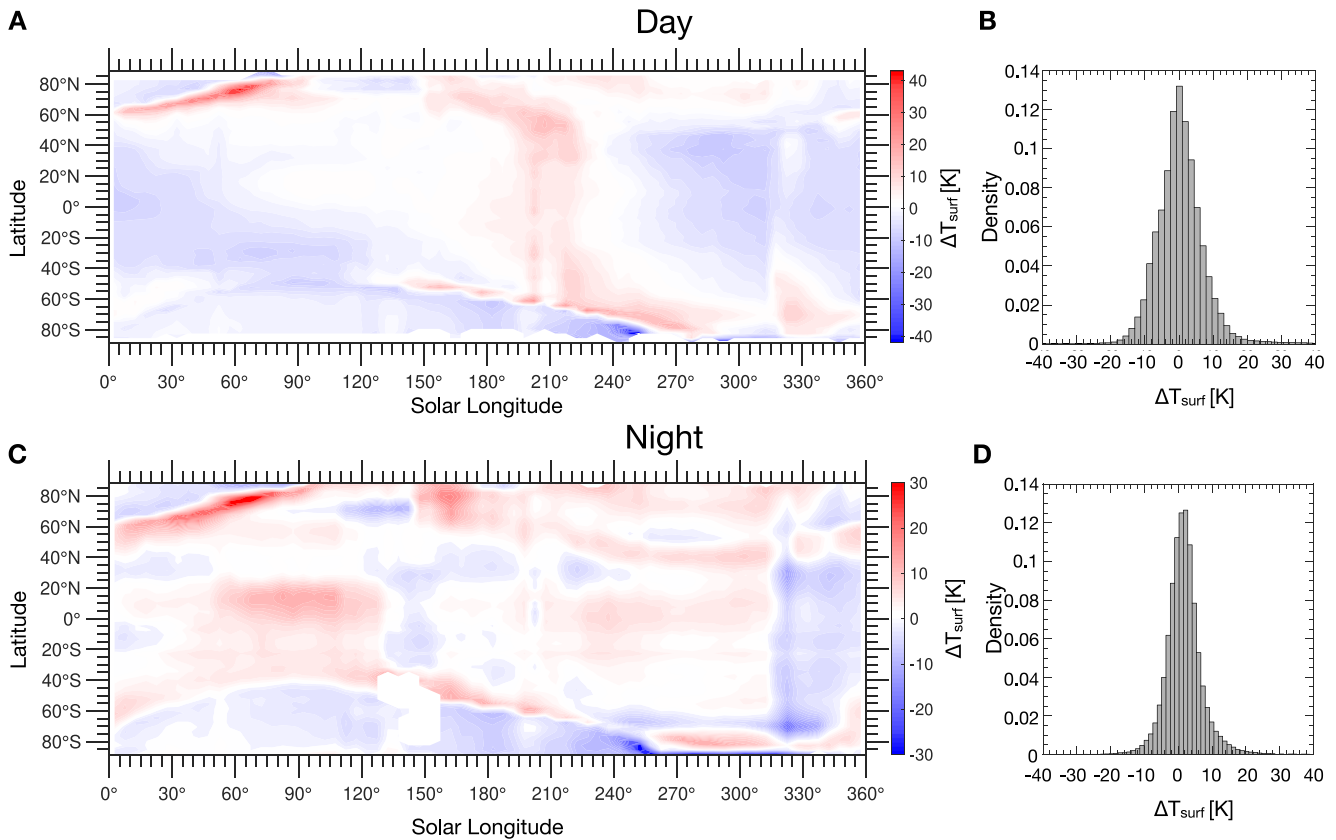
Figure 10. (a) Comparison between the zonally averaged surface temperatures made by Thermal Emission Spectrometer (TES) during MY 26 with grid-box averaged surface temperatures computed by the PCM during daytime (2 p.m.). (b) Distribution of the difference between the PCM and TES. Panels (c and d) same but for the night (2 a.m.). The ±30 K errors in the polar regions are related to the CO_2 caps that retreat earlier in the PCM compared to the observations.

consistent, even though small offsets can appear. We have quantified this difference over the year and planet by comparing the zonally average surface temperature measured by TES over MY 26 (M. D. Smith, 2004) to the values computed by the PCM. As TES values in M. D. Smith (2004) are binned by 3° × 3° of latitudes and longitudes, and 5° of L_s, we have compared these values to the grid-box averaged values given by the PCM. The comparison for daytime (2 p.m.) and nighttime (2 a.m.) is presented in Figure 10.

The PCM generally slightly overestimates surface temperature by ∼3–4 K during summer and underestimates by ∼3–4 K during winter. On average, during the year, the PCM marginally overestimates the surface temperature by +0.5 K (±6 K at 1-σ) during the day, and by 1.5 K (±6 K at 1-σ) during the night. These differences were also present in the former PCM without the parameterization and do not come from our work. In the polar regions, the differences come from an earlier retreat of the CO_2/H_2O ice cap predicted by the model which could be associated with an underestimation of the ice's albedos used in this study (see Table 2). However, as discussed later in Section 5.2, the albedos used here predict well the distribution of frost observed on slopes. Elsewhere, the differences might be related to the vertical representation of dust/water in the PCM as the temperature differences (outside of polar regions) are mostly found during periods of high opacity (e.g., L_s = 180°–210°, Figure 10a) Such conclusions can be extended to slope temperatures. Previous sections have shown that these temperatures were very sensitive to the slope azimuth and its thermal inertia. Nevertheless, we found a good agreement between our model and the observations. The agreement is better for short-scale topography (e.g., small crater, Figures 7 and 9) than significant topographic gradients (e.g., Valles Marineris, volcanoes, Figure 6) where slope winds can significantly impact the slope energy budget (Spiga et al., 2011).

These tests validate the overall good agreement between our model and the slope temperatures. However, we acknowledge that we cannot fully validate the surface temperatures on all slopes with our parameterization because of the difficulty of correcting the phase shift induced by the East-West components of the slopes and

the under-mesh heterogeneity for the surface properties which can lead to differences up to 10–15 K between the model and the observations as presented by Figures 6, 7, and 9 which are representatives of the error made. Again, the aim of this sub-grid parameterization is not to significantly improve the mesh-averaged surface temperature prediction, but to model local slope effects interacting with the full GCM. The fact that temperature prediction at grid-box levels is not significantly improved reflects the fact that the global climate is not affected by its slope microclimates as detailed in Section 6.1. However, the model can now be better used to investigate slope effects. Furthermore, the purpose of our parameterization is to represent the average thermal behavior of the slopes (diurnal average temperatures, minimum and maximum temperatures) and cannot fully simulate the instantaneous behavior. This is why we validate in the next section our parameterization with the observation of seasonal frost, which can theoretically be correctly represented by the parameterization.

### 5.2. Modeling the Distribution of Seasonal Frost on Slopes

5.2.1. Temporal Distribution

We now compare the distribution of seasonal CO_2 and H_2O frosts on slopes with the predictions of the PCM. For this validation, we used the frost detections made by OMEGA (Observatoire pour la Minéralogie, l'Eau, les Glaces et l'Activité) and CRISM (Compact Reconnaissance Imaging Spectrometer for Mars) instruments as reported in Vincendon, Forget, and Mustard (2010), Vincendon, Mustard, et al. (2010), and Vincendon (2015). These detections were made using near-infrared spectroscopy in the afternoon, and correspond to seasonal frost. Hence, diurnal frost forming during the night and sublimating during the early morning is not considered (Khuller et al., 2021; Lange et al., 2022; Piqueux et al., 2016). These observations are compared with the prediction of CO_2 and H_2O ice stability on a 30° pole-facing slope retrieved from the PCM simulations at the same local time, that is, 2 p.m. Following Vincendon, Mustard, et al. (2010), we assume that CO_2 ice is stable and should be detected by CRISM/OMEGA at a given latitude if the CO_2 ice thickness predicted on the slope by the PCM exceeds 200 µm at $L_s \geq 120°$, 1,000 µm before. The threshold used is higher for $L_s \leq 120°$ because of the low signal-to-noise ratio on the slope at this time of the Martian year. Imposing a lower threshold (e.g., 100 µm) would lead to an earlier condensation by ∼5° of L_s, and an equatorward extent of the distribution by 3° of latitude. For H_2O ice, the thickness threshold is set to 5 µm (Vincendon, Forget, & Mustard, 2010). The comparison is presented in Figure 11.

CO_2 ice: The PCM with the sub-grid slope parameterization predicts CO_2 ice on 30° pole-facing slopes in the southern hemisphere up to 33°S while the former PCM could predict CO_2 ice on flat surfaces as low ∼48°S. This new latitudinal extent is consistent with observations by CRISM and OMEGA which detected CO_2 frost on south-facing slopes up to 32.3°S. We observed an overall very good agreement between our modeling predictions and actual CO_2 detections.

The timing of condensation/sublimation is consistent with the observations, even though both start slightly too early (by 5–10° of L_s). Vincendon, Mustard, et al. (2010) showed that the beginning of condensation is sensitive to the amount of dust in the atmosphere, the presence of ice in the subsurface, and the thermal inertia of the surface. Dust is set to the observations of Montabone et al. (2015) and can not be tuned to match the observations. The subsurface ice is predicted to be stable at a depth of ∼1 m in the 35°–45°S band (see Section 3.1.3). At such depth, subsurface ice has almost no impact on the surface energy budget and CO_2 ice distribution. Hence, the difference between our model and the CO_2 ice observations suggests shallower ice that is not predicted by our ice stability model. One can also delay the beginning of the modeled CO_2 condensation/sublimation by modifying slope surface properties. However, no clear constraints exist for these properties as some slopes exhibit low thermal inertia (Tebolt et al., 2020), favoring the condensation of CO_2; while some slopes reveal high-thermal inertia bedrock exposures (Edwards et al., 2009) which delay the formation of CO_2 frost. Finally, one should note that the difference in the timing of condensation is observed at $L_s \leq 120°$, a time when fewer ice observations are available because of the low illumination in this period, lowering the signal-to-noise ratio, and potentially preventing some detections.

Here, our model matches well the observations without relying on subsurface ice as in Vincendon, Mustard, et al. (2010). This may be due to the fact that our model considers the surrounding plains that warm the atmosphere, increasing the downwelling infrared flux and therefore the surface temperature. Such effects, which were not considered in Vincendon, Mustard, et al. (2010), and their consequences are discussed in Section 6.1 and are more detailed in a companion paper (Lange, Forget, Vincendon, et al., 2023, accepted for publication in GRL).
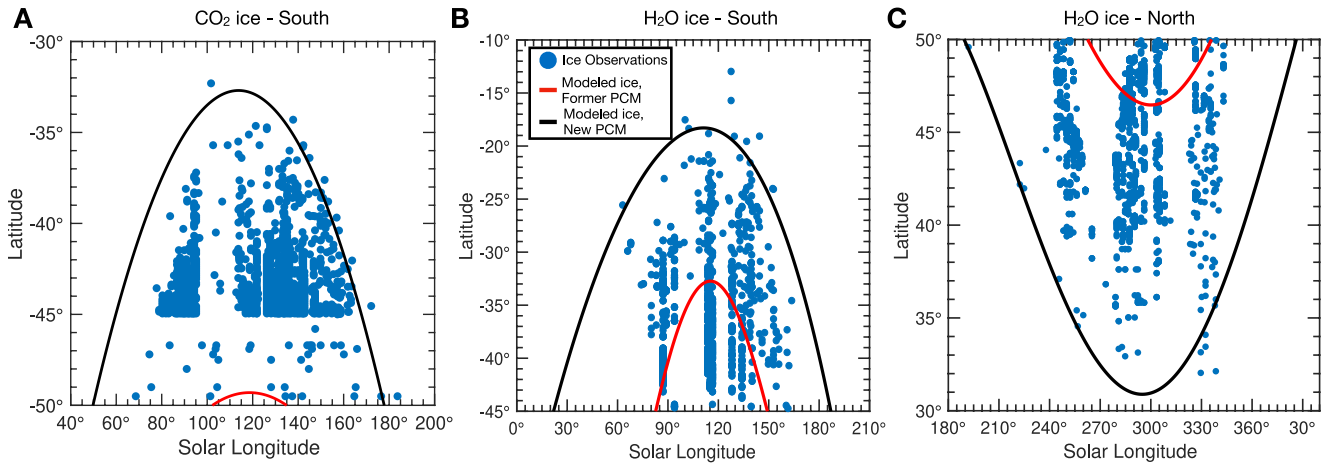
Figure 11. Latitudinal distribution of (a) CO_2 and (b and c) H_2O frost versus solar longitude L_s. Blue points correspond to the observations of frost by CRISM/OMEGA (Vincendon, 2015; Vincendon, Forget, & Mustard et al., 2010; Vincendon, Mustard, et al., 2010). The red curve is the prediction of frost stability by the former PCM without the sub-grid slope parameterization, and the dark curve is the prediction of frost stability on a 30° pole-facing slope. The maximum extent of CO_2 ice predicted by the PCM is in the East of Hellas (100–150°E). CO_2 ice is predicted if the CO_2 frost thickness exceeds 200 μm at $L_s \geq 120°$, 1,000 μm before. H_2O ice is predicted at a given latitude by the PCM if the H_2O frost thickness exceeds 5 μm. H_2O frost shown in (b) is located in the band 0°–60°E, and in the band 280°–340°E for (c). Similar conclusions can be drawn at other longitudes. The PCM outputs are retrieved at 2 p.m., that is, the local time when most CRISM/OMEGA data were acquired.

H_2O ice: Similar conclusions can be drawn when looking at the predicted latitude-season stability diagram for H_2O ice (Figures 11b and 11c). The latitudinal extent of H_2O ice is well predicted (as low as 30°N and 18°S vs. 48°N and 33°S for the former PCM), even if few deposits at low latitudes (e.g., the one close in Valles Marineris at latitude 12.7°S) are not predicted by our model. In our experiment, the broadband albedo of H_2O ice is set to 0.33 as it enables a good fit of the seasonal water cycle in the PCM (Naar et al., 2021). Similarly to Vincendon, Forget, and Mustard (2010), increasing the albedo leads to a delay by a few degrees of L_s in the sublimation of the deposits. The sublimation of these deposits is also sensitive to wind speed. Here, this speed might be underestimated because the model does not compute slope winds although this should not significantly impact our results (Vincendon, Forget, & Mustard, 2010). The beginning of the condensation of H_2O is also too early by ∼10° of L_s in the PCM compared to the observations, as for the CO_2 ice. This might be due to an observational bias in the autumn high latitude water ice detections at these longitudes (Vincendon, Forget, & Mustard, 2010), and a bias of our model that might underestimate surface temperature at this season as reported previously. One should note that our results are quite similar to those obtained by Vincendon, Forget, and Mustard (2010).

5.2.2. Spatial Distribution

We also validate our parameterization by comparing the spatial distribution of CO_2 and H_2O ice observed by CRISM/OMEGA with our model. Results are presented in Figure 12.

CO_2 ice: Similarly to Vincendon, Mustard, et al. (2010), the latitudinal stability limit of CO_2 ice on a 30° pole-facing slope (Figure 12a) varies with longitude, with a mean value of 33°. Below 33°, ice might be present but as thin deposits (<100 μm). CO_2 ice between −120° and −60°E, that is, Thaumasia regions, is predicted to be thinner compared to the rest of the longitudes because of the higher altitude in this place, and thus the lower temperature of CO_2 condensation. Our statistics of sub-grid slopes also suggest that the lack of CO_2 ice detections in this region might be linked to the few numbers of steep (>30°) south-facing slopes in this area. Interestingly, we found that CO_2 ice detections by CRISM/OMEGA correlate with thick CO_2 ice predicted by the model, while Vincendon, Mustard, et al. (2010) proposed that deposits of few hundred of microns should be detected. The overall agreement validates our model for CO_2 deposits. Few points are not predicted (e.g., the detection at 32.3°S on the East of Hellas) but this might be linked to favorable local conditions or the resolution of our model (3.75° of latitude) which might be not precise enough to differentiate what happens within a very few degrees of latitude. One can note that the model does not predict ice in Hellas Basin whereas it has been observed on flat surfaces (Piqueux et al., 2016) and on the rare steep slopes present at this place (Vincendon, Mustard, et al., 2010). This is because of a systematic error in the Mars PCM (also present without the parameterization of slopes) which is under investigation.
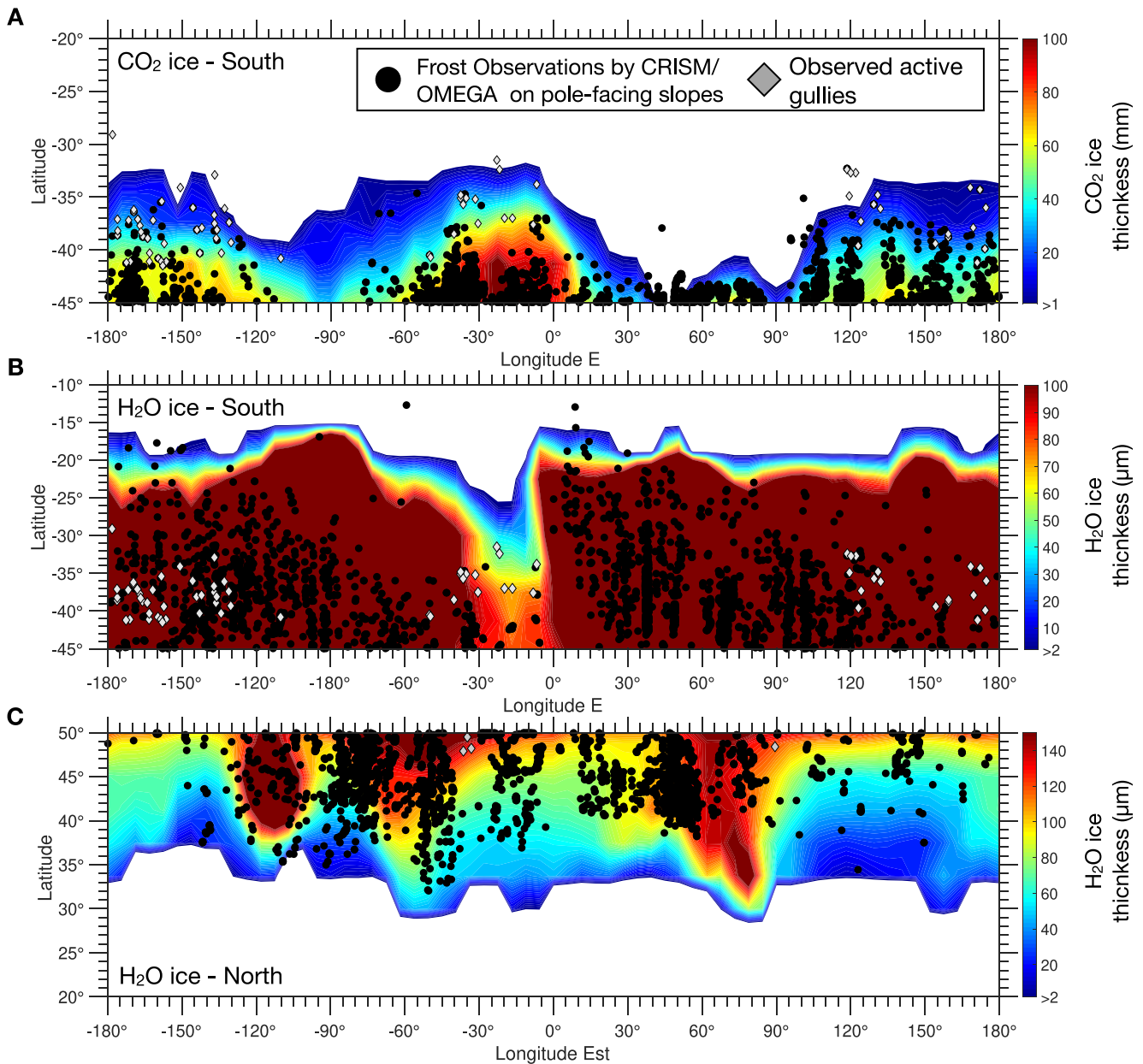
Figure 12. Spatial distribution of CO_2 and H_2O on a 30°pole-facing slopes predicted by our model and ice detection made by CRISM and OMEGA (black dots). (a) CO_2 ice in the Southern Hemisphere; (b) H_2O ice in the Southern Hemisphere; (c) H_2O ice in the Northern Hemisphere. The thicknesses presented here are the maximum frost thickness across the entire Martian year. Observed active gullies reported by Dundas et al. (2022) are represented by gray diamonds. The PCM outputs are retrieved at 2 p.m., that is, the local time when most CRISM/OMEGA data were acquired.

H_2O ice: Similar conclusions can be drawn when looking at the spatial distribution of water ice. In the South (Figure 12b), our model reproduces well the observations, with notably the dry area in the band $-40°$ to $0°E$ where thinner frost (or no frost) is expected, as confirmed by the low amount of detections in this area. This is a consequence of the western jet on the eastern side of the Tharsis bulge (Joshi et al., 1994, 1995) leading to a dryer atmosphere (less water vapor available to form H_2O frost) (Vincendon, Forget, & Mustard, 2010). Again, the model predicts ice in the Thaumasia region which is not observed. The same explanations as those mentioned above for CO_2 ice, similar to those given by Vincendon, Forget, and Mustard (2010), can be given. Locally, the latitudinal stability is higher than what is predicted by Vincendon, Forget, and Mustard (2010) (e.g., $-180°$ to $-150°E$) and explains some low latitude ice detections. In the North, the model predicts well the areas where numerous detections are made, as well as dry areas (e.g., $-180°$ to $-150°E$) where fewer ice deposits are observed by CRISM/OMEGA.

6. Discussions and Perspectives

6.1. Relationship Between the Atmosphere and the Slope Microclimates

One may first wonder if the slope microclimates impact the global climate. It is assumed here that the atmosphere sees an average of the sub-grid fields, weighted by the cover fraction. In Section 2, we showed that the predominant sub-surface is the flat one (non-flat sub-grid surfaces represent 5% of the overall area). A significant impact of the slope microclimates on the global climate was thus not expected. We checked this assumption by comparing PCM runs with and without this parameterization and found little differences. For instance, the relative difference of the total mass of CO_2 ice that condenses during the year between simulation with and without the sub-grid slope parameterization is lower than 1%. Similar conclusions can be drawn for the amount of H_2O ice, and the total amount of H_2O in the atmosphere. This is because (a) steep slopes, which accumulate a larger amount of frost compared to flat surfaces, are sparse and of limited length (tens or hundreds of meters, Aharonson & Schorghofer, 2006); (b) regionally, some areas with a lot of pole-facing slopes have an excess of ice when considering the parameterization, but this is balanced by areas with a lot of equatorward-facing slopes, which have lower amounts of ice.

To date, slope microclimates have mostly been explored with 1D models (e.g., Aharonson & Schorghofer, 2006; Vincendon, Mustard, et al., 2010) which neglect contribution from the large-scale atmosphere dynamic. Therefore, one may wonder about the impact of the global climate on slope microclimates. In the 1D PCM used in Vincendon, Forget, and Mustard et al. (2010) and Vincendon, Mustard, et al. (2010), the atmosphere is in radiative equilibrium with the surface studied. For a pole-facing slope, the atmosphere above it is therefore cold. However, in our 3D model, we assume that the atmosphere is horizontally mixed at the scale of the slopes. The atmosphere sees an average of sloped and flat sub-grid surfaces. As steep sloped terrains represent actually a small percentage of the overall surface of Mars (see Section 2), the atmosphere is mostly in equilibrium with the warmer flat sub-grid surface. Hence, in the 3D model, the air close to cold sloped surfaces is warmer than in the 1D model as it is warmed by the nearby warm plains. This legitimizes the computation of other models (e.g., Aharonson & Schorghofer, 2006; Kieffer, 2013; Mellon & Phillips, 2001; Schorghofer & Edgett, 2006) which used the same atmospheric infrared radiation for flat surfaces and steep slopes. Also, during winter, warm air is brought above pole-facing slopes because of the subsidence from the Hadley cell at mid and subtropical latitudes, which leads to adiabatic heating of the atmosphere (Barnes et al., 2017). This warmer atmosphere increases the downwelling infrared flux and thus modifies the amount CO_2/H_2O ice condensing on the surface. Note that this effect is mostly pronounced for areas with a strong thermal contrast between the slopes and the flat surfaces and is thus most significant for low-latitude slopes ($\leq\pm45°N$). These two effects increase the slope energy budget by nearly 10 W m^{-2}, with significant consequences for CO_2 frost extent. A more accurate description and demonstration of these two effects and their consequences are discussed in a companion paper (Lange, Forget, Vincendon, et al., 2023, accepted for publication in GRL). As discussed in Sections 3.4.4 and 3.4.5, this assumption of a "shared" atmosphere, mostly in equilibrium with the flat surfaces, might lead to a small overestimation of the downwelling infrared flux, as cold air can, for instance, be confined within a crater by katabatic slope winds during the night and early morning. This might explain why our model has a too early starting of the CO_2 sublimation (Figure 11) compared to the observations, but our choice is reasonable to study small/medium topographic relief.

6.2. Reappraisal of the Frost Thicknesses and Consequences for the Activity of Gullies

Estimating the thickness of seasonal frosts (H_2O or CO_2 ice) on slopes is an important constraint for models of gully activity associated with sublimation processes (Diniega et al., 2021; Dundas, McEwen, et al., 2019). No measurements of these thicknesses have been made and they have only been estimated by 1D models to date. Such studies only estimate frost thickness for specific locations and not at a global scale (e.g., Khuller et al., 2021; Schorghofer & Edgett, 2006; Vincendon, 2015). We provide in Figure 12 a complete mapping (220 × 330 km of resolution) of the expected maximum CO_2 frost thickness across the year for 30° pole-facing slopes. Compared to most of the 1D models used in the literature, our model with the sub-grid slope parameterization takes into account the seasonal CO_2 cycle that has been validated against observations, CO_2 depletion at polar latitudes, and the effects of large-scale meteorology. The seasonal frost thickness logically decreases with latitude, from a few mm at 33°S ($\pm3°$ of latitude due to the model resolution) to a few tens of cm at 45°S. Equatorward of 33°S, the model predicts ~0.1 mm frost forming during the night which disappears during the morning, as observed

by Khuller et al. (2021) and Lange et al. (2022). Our model predicts larger ice thicknesses for mid and high latitudes (tens of cm). Interestingly, we find that in the southern hemisphere, the amount of CO_2 that condenses on a 30° pole-facing slope has a similar frost thickness to the amount that condenses on flat terrain at about 10 degrees of latitude lower. For example, at 41°S, ~5 cm of frost can form on a 30° pole-facing slope, which is the same amount as that observed at the edge of the seasonal cap at ~48°S (Litvak et al., 2007). This is not observed in the Northern Hemisphere because of the shorter winter for the current eccentricity of Mars. However, as mentioned previously, this phenomenon will not impact the global mass of CO_2 that will condense during the winter because these very steep slopes are rare on Mars and of limited length (tens or hundreds of meters, Aharonson & Schorghofer, 2006). The longitudinal variations of frost thickness reflect the variations in surface properties (albedo, thermal inertia), and altitude. For water, we find a distribution similar to that of Vincendon, Forget, and Mustard (2010) who used a 1D model coupled with precipitation maps obtained in 3D. The frost thicknesses obtained are larger in our model by ten's/hundreds of micrometers because the water cycle of the 3D model has been improved (Naar et al., 2021) and is now wetter compared to the version used by Vincendon, Forget, and Mustard (2010).

These new frost maps, compared to the map of active gullies, give us important information for modeling gully activity on Mars. Indeed, near-infrared observations suggest that active gullies are highly correlated to the presence of CO_2 frost (Vincendon, 2015). By constructing high-resolution surface temperature maps with the method described in Section 3.3 (Figures 12 and 13), we can see that the location of most of the active gullies indeed coincides with slopes where CO_2 condensation occurs. More specifically, we found that the model predicts frost on 30° slopes on 91% of the active gully sites and 86% of all gully sites in the South. In the North, this percentage is reduced to 56% for active sites and only 9% for all gullies. Our derived values are upper limits as the amount of ice is predicted for steep (≥30°) pole-facing slopes for which the frost is most stable. Using a lower slope angle would hence reduce the statistics presented there. Nevertheless, our numbers are consistent with the same statistics derived in Khuller et al. (2021). Hence, both observations and modeling suggest that the activity of gullies is mostly related to processes involving CO_2 ice. However, the model does not predict a significant amount of CO_2 ice (a few cm thick, Figure 12a), thus disfavoring models that require a significant amount of ice (e.g., Diniega et al., 2013, although this model is for linear gullies which are mostly found above 45° latitude, where thicker ice is expected), and promoting processes that do not need significant amounts of ice (less than a cm) to enable fluidization (de Haas et al., 2019). Note that all active gullies closest to the equator are not necessarily correlated with the presence of CO_2 according to the model and observations (Khuller et al., 2021; Vincendon, 2015), but are correlated with the presence of water ice frost. The absence of CO_2 frost predicted by our model in these locations might be explained by local effects: steep slopes (e.g., 35°, not modeled in our parameterization), shadowing induced by surrounding terrains (e.g., Schorghofer, 2020), and low thermal inertia. All of these effects can create cold spots where CO_2 condenses but are not modeled here (see Section 3.4). Yet, the possible contribution of water ice-related mechanisms can not be ruled out. This preliminary analysis will be extended to present and past orbital configurations in future dedicated studies.

7. Conclusions

The objectives of this paper are to propose a parameterization to simulate slope microclimates in coarse grid GCM, implement it in the Mars Planetary Climate Model, and discuss the impact of these microclimates on the global climate of Mars and on the activity of some surface processes. The main conclusions of this investigation are:

1. We can simulate the slope microclimates by representing each Mars GCM cell as a set of flat and sloped sub-grid surfaces on which we compute the surface and subsurface temperatures, as well as CO_2 and H_2O ice deposits (Figure 1).
2. To correctly represent the properties of the sub-grid sloped surfaces, we have demonstrated that any given slope with a slope angle θ and azimuth ψ can be on average thermally represented (same surface temperature ranges and averages) by a slope $\mu = \theta \cos(\psi)$ that is either North-facing if $\mu > 0$, or South-facing if $\mu < 0$ (Figure 2);
3. Using seven values for μ is enough to represent accurately the sub-grid slopes (Figure 3). For the quasi-totality of the Mars PCM cells, the predominant sub-grid surface is the flat one (Figure 4);
4. This parameterization improves the prediction of observed surface temperatures created by sub-grid heterogeneities compared to the former version of the PCM (Figures 6, 7, 9, and 10).
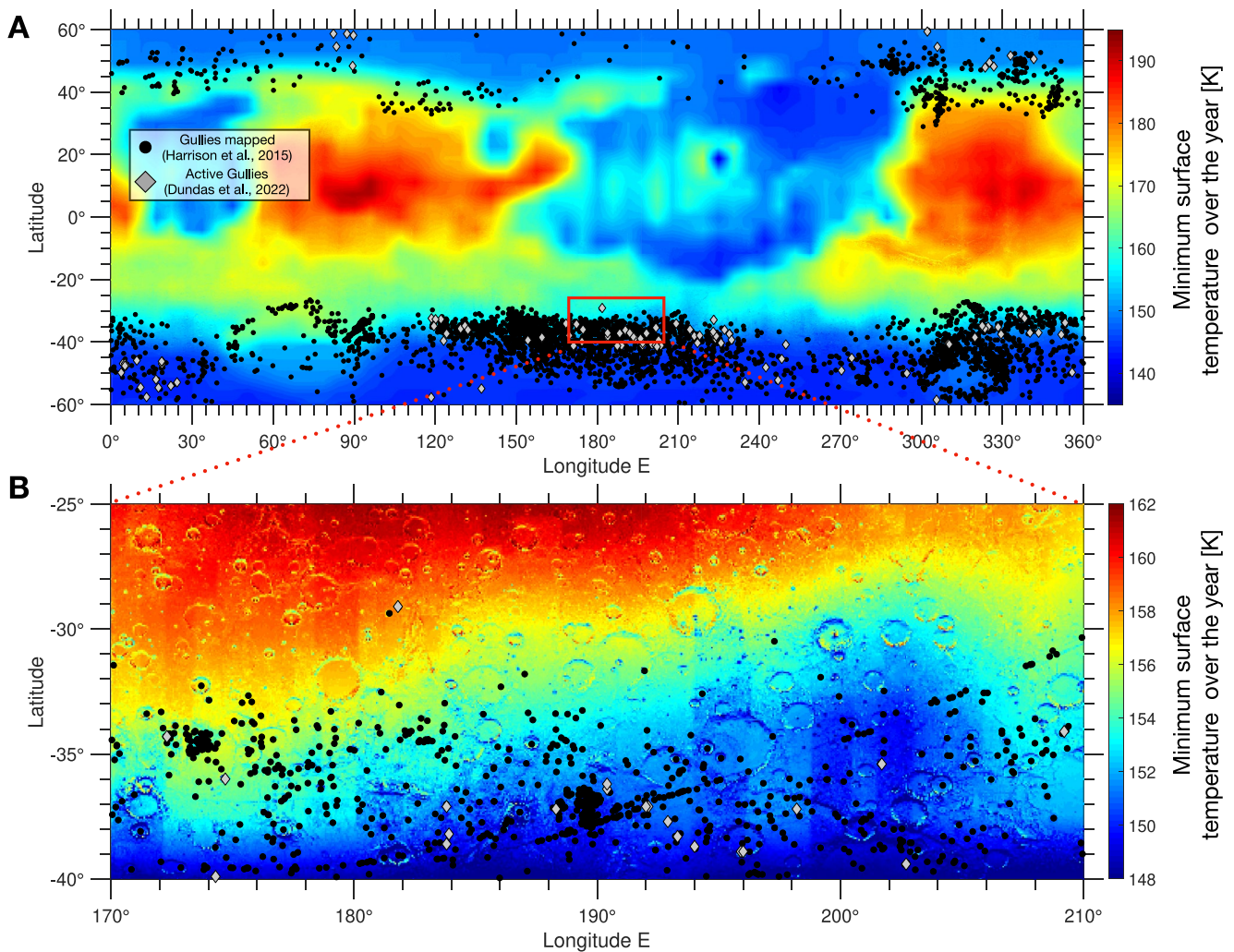
Figure 13. Minimum surface temperature computed by the PCM with the sub-grid slope parameterization between 60°S and 60°N. The Gullies sites mapped by Harrison et al. (2015) are represented by the black dots, and the active gullies sites reported in Dundas et al. (2022) by the gray diamonds. No MOLA background has been added to the plot. Panel (b) is a close-up of panel (a) between 45° and 20°S, 170°–210°E.

5. The comparison between slope surface temperatures measured by THEMIS and our model shows a good agreement: the differences between the model and the observations are lower than 5 K on average (Figures 7 and 9). These differences arise from the model limits detailed in Section 3.4.

6. The spatial and temporal distribution of CO_2 and H_2O frost on pole-facing slopes obtained from our model agree well with measurements made by CRISM and OMEGA (Figures 11 and 12).

7. While steep slopes can accumulate a significant amount of CO_2 and H_2O ice (Figure 12), slope microclimates do not impact the seasonal water and CO_2 cycles on a global scale as steep slopes are sparse on Mars. The extra amount of frost that condenses because of the sub-grid parameterization is less than 1% of the total mass of the ice on the planet;

8. Warm plains around steep pole-facing slopes heat the atmosphere, increasing the incident infrared flux, preventing the formation of CO_2 ice at low latitudes (Section 6.1);

9. We provide for the first time a global map of CO_2 frost thicknesses and a revised map of H_2O frost thicknesses on steep ($\geq 30°$) slopes (220×330 km of resolution), which present larger deposits than previously reported (Figure 12);

10. Our model (Figures 12 and 13), complemented by specific observations at near-infrared (Vincendon, 2015) suggests that the activity of gullies is mostly related to processes involving CO_2 ice, but rules out processes that require a significant amount of ice (Section 6.2);

This new model opens the way to novel modeling studies for surface-atmosphere interactions in the present but also past climates, allowing a better understanding of the geological record observed today. Future improvements of the model are underway, including the addition of sub-grid slope winds. Finally, our parametrization proposed here on Mars is not specific to this planet but can be adapted to bodies whose energy balance is dominated by radiative exchanges (for instance, Pluto, Triton, etc).

Data Availability Statement

THEMIS, TES infrared images, and MOLA data can be retrieved from the Planetary Data System (Alexey, 2020; Christensen, 2002; D. Smith et al., 1999) at https://pds-atmospheres.nmsu.edu. Frost detections are from Vincendon, Forget, and Mustard (2010), Vincendon, Mustard, et al. (2010), and Vincendon (2015) Gullies site reported in the last Figure can be obtained from Dundas, McEwen et al. (2019), Dundas et al. (2022), and Harrison et al. (2015). Data files for figures used in this analysis are available in a public repository, see Lange, Forget, Dupont, et al. (2023). The Mars PCM used in this work can be downloaded with documentation from the SVN repository at https://svn.lmd.jussieu.fr/Planeto/trunk/LMDZ.MARS/. More information and documentation are available at http://www-planets.lmd.jussieu.fr.

References

Aharonson, O., & Schorghofer, N. (2006). Subsurface ice on Mars with rough topography. *Journal of Geophysical Research*, *111*(E11), E11007. https://doi.org/10.1029/2005JE002636

Aharonson, O., Schorghofer, N., & Gerstell, M. F. (2003). Slope streak formation and dust deposition rates on Mars. *Journal of Geophysical Research*, *108*(E12), 5138. https://doi.org/10.1029/2003JE002123

Ahern, A. A., Rogers, A. D., Edwards, C. S., & Piqueux, S. (2021). Thermophysical properties and surface heterogeneity of landing sites on Mars from overlapping thermal emission imaging system (THEMIS) observations. *Journal of Geophysical Research: Planets*, *126*(6), e2020JE006713. https://doi.org/10.1029/2020JE006713

Alexey, P. (2020). Mars global surveyor thermal emission spectrometer atmospheric recalibration bundle [Dataset]. NASA Planetary Data System. https://doi.org/10.17189/XHQZ-ZW13

Bandfield, J. L. (2007). High-resolution subsurface water-ice distributions on Mars. *Nature*, *447*(7140), 64–67. https://doi.org/10.1038/nature05781

Bandfield, J. L., & Feldman, W. C. (2008). Martian high latitude permafrost depth and surface cover thermal inertia distributions. *Journal of Geophysical Research*, *113*(E8), E08001. https://doi.org/10.1029/2007je003007

Bandfield, J. L., & Smith, M. D. (2003). Multiple emission angle surface-atmosphere separations of thermal emission spectrometer data. *Icarus*, *161*(1), 47–65. https://doi.org/10.1016/S0019-1035(02)00025-8

Barnes, J. R., Haberle, R. M., Wilson, R. J., Lewis, S. R., Murphy, J. R., & Read, P. L. (2017). The global circulation. In *The atmosphere and climate of Mars* (pp. 229–294). Cambridge University Press. https://doi.org/10.1017/9781139060172.009

Boynton, W., Feldman, W., Mitrofanov, I., Evans, L., Reedy, R., Squyres, S., et al. (2004). The Mars Odyssey Gamma-Ray Spectrometer instrument suite. *Space Science Reviews*, *110*(1/2), 37–83. https://doi.org/10.1023/b:spac.0000021007.76126.15

Boynton, W. V., Feldman, W. C., Squyres, S. W., Prettyman, T. H., Bruckner, J., Evans, L. G., et al. (2002). Distribution of hydrogen in the near surface of Mars: Evidence for subsurface ice deposits. *Science*, *297*(5578), 81–85. https://doi.org/10.1126/science.1073722

Carrozzo, F. G., Bellucci, G., Altieri, F., D'Aversa, E., & Bibring, J. P. (2009). Mapping of water frost and ice at low latitudes on Mars. *Icarus*, *203*(2), 406–420. https://doi.org/10.1016/j.icarus.2009.05.020

Christensen, P. R. (2002). ODYSSEY THEMIS IR PBT V2.0 [Dataset]. NASA Planetary Data System. https://doi.org/10.17189/1520354

Christensen, P. R., Bandfield, J. L., Bell, J. F., III, Gorelick, N., Hamilton, V. E., Ivanov, A., et al. (2003). Morphology and composition of the surface of Mars: Mars Odyssey THEMIS results. *Science*, *300*(5628), 2056–2061. https://doi.org/10.1126/science.1080885

Christensen, P. R., Bandfield, J. L., Hamilton, V. E., Ruff, S. W., Kieffer, H. H., Titus, T. N., et al. (2001). Mars Global Surveyor Thermal Emission Spectrometer experiment: Investigation description and surface science results. *Journal of Geophysical Research*, *106*(E10), 23823–23871. https://doi.org/10.1029/2000je001370

Christensen, P. R., Jakosky, B. M., Kieffer, H. H., Malin, M. C., McSween, H., Nealson, K., et al. (2004). *The Thermal Emission Imaging System (THEMIS) for the Mars 2001 Odyssey Mission*. (pp. 85–130). Springer Netherlands. https://doi.org/10.1007/978-0-306-48600-5_3

Colaïtis, A., Spiga, A., Hourdin, F., Rio, C., Forget, F., & Millour, E. (2013). A thermal plume model for the Martian convective boundary layer. *Journal of Geophysical Research: Planets*, *118*(7), 1468–1487. https://doi.org/10.1002/jgre.20104

Costard, F., Forget, F., Mangold, N., & Peulvast, J. P. (2002). Formation of recent Martian debris flows by melting of near-surface ground ice at high obliquity. *Science*, *295*(5552), 110–113. https://doi.org/10.1126/science.1066698

de Haas, T., McArdell, B. W., Conway, S. J., McElwaine, J. N., Kleinhans, M. G., Salese, F., & Grindrod, P. M. (2019). Initiation and flow conditions of contemporary flows in Martian gullies. *Journal of Geophysical Research: Planets*, *124*(8), 2246–2271. https://doi.org/10.1029/2018JE005899

de Vrese, P., Schulz, J.-P., & Hagemann, S. (2016). On the representation of heterogeneity in land-surface–atmosphere coupling. *Boundary-Layer Meteorology*, *160*(1), 157–183. https://doi.org/10.1007/s10546-016-0133-1

Dickinson, R., Henderson-Sellers, A., Kennedy, P., & Wilson, M. (1986). Biosphere-atmosphere transfer scheme (BATS) for the NCAR Community Climate Model (Technical Report). https://doi.org/10.5065/D6668B58

Diez, B., Feldman, W., Maurice, S., Gasnault, O., Prettyman, T., Mellon, M., et al. (2008). H layering in the top meter of Mars. *Icarus*, *196*(2), 409–421. https://doi.org/10.1016/j.icarus.2008.02.006

Diniega, S., Bramson, A. M., Buratti, B., Buhler, P., Burr, D. M., Chojnacki, M., et al. (2021). Modern Mars' geomorphological activity, driven by wind, frost, and gravity. *Geomorphology*, *380*, 107627. https://doi.org/10.1016/j.geomorph.2021.107627

Diniega, S., Hansen, C., McElwaine, J., Hugenholtz, C., Dundas, C., McEwen, A., & Bourke, M. (2013). A new dry hypothesis for the formation of Martian linear gullies. *Icarus*, *225*(1), 526–537. https://doi.org/10.1016/j.icarus.2013.04.006

Diniega, S., Hansen, C. J., Allen, A., Grigsby, N., Li, Z., Perez, T., & Chojnacki, M. (2019). Dune-slope activity due to frost and wind throughout the North Polar Erg, Mars. In *Martian gullies and their Earth analogues*. Geological Society of London. https://doi.org/10.1144/SP467.6

Dozier, J., & Frew, J. (1990). Rapid calculation of terrain parameters for radiation modeling from digital elevation data. *IEEE Transactions on Geoscience and Remote Sensing*, *28*(5), 963–969. https://doi.org/10.1109/36.58986

Dufresne, J.-L., Fournier, R., Hourdin, C., & Hourdin, F. (2005). Net exchange reformulation of radiative transfer in the CO_2 15-μm band on Mars. *Journal of the Atmospheric Sciences*, *62*(9), 3303–3319. https://doi.org/10.1175/jas3537.1

Dundas, C. M., Becerra, P., Byrne, S., Chojnacki, M., Daubar, I. J., Diniega, S., et al. (2021). Active Mars: A dynamic world. *Journal of Geophysical Research: Planets*, *126*(8), e2021JE006876. https://doi.org/10.1029/2021JE006876

Dundas, C. M., Bramson, A. M., Ojha, L., Wray, J. J., Mellon, M. T., Byrne, S., et al. (2018). Exposed subsurface ice sheets in the Martian mid-latitudes. *Science*, *359*(6372), 199–201. https://doi.org/10.1126/science.aao1619

Dundas, C. M., Conway, S. J., & Cushing, G. E. (2022). Martian gully activity and the gully sediment transport system. *Icarus*, *386*, 115133. https://doi.org/10.1016/j.icarus.2022.115133

Dundas, C. M., McEwen, A. S., Diniega, S., Hansen, C. J., Byrne, S., & McElwaine, J. N. (2019). The formation of gullies on Mars today. *Geological Society of London Special Publications*, *467*(1), 67–94. https://doi.org/10.1144/SP467.5

Dundas, C. M., Mellon, M. T., Conway, S. J., & Gastineau, R. (2019). Active boulder movement at high Martian latitudes. *Geophysical Research Letters*, *46*(10), 5075–5082. https://doi.org/10.1029/2019gl082293

Edwards, C. S., Bandfield, J. L., Christensen, P. R., & Fergason, R. L. (2009). Global distribution of bedrock exposures on Mars using THEMIS high-resolution thermal inertia. *Journal of Geophysical Research*, *114*(E11), E11001. https://doi.org/10.1029/2009JE003363

Feistel, R., & Wagner, W. (2007). Sublimation pressure and sublimation enthalpy of H_2O ice Ih between 0 and 273.16 K. *Geochimica et Cosmochimica Acta*, *71*(1), 36–45. https://doi.org/10.1016/j.gca.2006.08.034

Feldman, W. C., Boynton, W. V., Tokar, R. L., Prettyman, T. H., Gasnault, O., Squyres, S. W., et al. (2002). Global distribution of neutrons from Mars: Results from Mars Odyssey. *Science*, *297*(5578), 75–78. https://doi.org/10.1126/science.1073541

Feldman, W. C., Prettyman, T. H., Maurice, S., Plaut, J. J., Bish, D. L., Vaniman, D. T., et al. (2004). Global distribution of near-surface hydrogen on Mars. *Journal of Geophysical Research*, *109*(E9), E09006. https://doi.org/10.1029/2003JE002160

Flato, G., Marotzke, J., Abiodun, B., Braconnot, P., Chou, S. C., Collins, W., et al. (2013). Evaluation of climate models. In T. F. Stocker, D. Qin, G.-K. Plattner, M. Tignor, S. K. Allen, J. Boschung, et al. (Eds.), *Climate Change 2013: The Physical Science Basis. Contribution Of Working Group I to the Fifth Assessment Report of the Intergovernmental Panel on Climate Change* (pp. 741–882). Cambridge University Press. https://doi.org/10.1017/CBO9781107415324.020

Forget, F. (1998). Improved optical properties of the martian atmospheric dust for radiative transfer calculations in the infrared. *Geophysical Research Letters*, *25*(7), 1105–1108. https://doi.org/10.1029/98GL50653

Forget, F., Hourdin, F., Fournier, R., Hourdin, C., Talagrand, O., Collins, M., et al. (1999). Improved general circulation models of the Martian atmosphere from the surface to above 80 km. *Journal of Geophysical Research*, *104*(E10), 24155–24175. https://doi.org/10.1029/1999JE001025

Forget, F., Hourdin, F., & Talagrand, O. (1998). CO_2 snow fall on Mars: Simulation with a general circulation model. *Icarus*, *131*(2), 302–316. https://doi.org/10.1006/icar.1997.5874

Giorgi, F., & Avissar, R. (1997). Representation of heterogeneity effects in earth system modeling: Experience from land surface modeling. *Reviews of Geophysics*, *35*(4), 413–437. https://doi.org/10.1029/97rg01754

Haberle, R. M., Forget, F., Colaprete, A., Schaeffer, J., Boynton, W. V., Kelly, N. J., & Chamberlain, M. A. (2008). The effect of ground ice on the Martian seasonal CO_2 cycle. *Planetary and Space Science*, *56*(2), 251–255. https://doi.org/10.1016/j.pss.2007.08.006

Hagedorn, B., Sletten, R. S., & Hallet, B. (2007). Sublimation and ice condensation in hyperarid soils: Modeling results using field data from Victoria Valley, Antarctica. *Journal of Geophysical Research*, *112*(F3), F03017. https://doi.org/10.1029/2006JF000580

Harrison, T. N., Osinski, G. R., Tornabene, L. L., & Jones, E. (2015). Global documentation of gullies with the Mars Reconnaissance Orbiter Context Camera and implications for their formation. *Icarus*, *252*, 236–254. https://doi.org/10.1016/j.icarus.2015.01.022

Head, J. W., & Marchant, D. R. (2003). Cold-based mountain glaciers on Mars: Western Arsia Mons. *Geology*, *31*(7), 641. https://doi.org/10.1130/0091-7613(2003)031<0641:cmgomw>2.0.co;2

Hébrard, E., Listowski, C., Coll, P., Marticorena, B., Bergametti, G., Määttänen, A., et al. (2012). An aerodynamic roughness length map derived from extended Martian rock abundance data. *Journal of Geophysical Research*, *117*(E4), E04008. https://doi.org/10.1029/2011JE003942

Hobbs, P. V. (1974). *Ice physics*. Oxford University Press.

Hobbs, S., Paull, D., & Clarke, J. (2013). The influence of slope morphology on gullies: Terrestrial gullies in Lake George as analogues for Mars. *Planetary and Space Science*, *81*, 1–17. https://doi.org/10.1016/j.pss.2012.10.009

Hourdin, F. (1992). A new representation of the absorption by the CO_2 15-μm band for a Martian general circulation model. *Journal of Geophysical Research*, *97*(E11), 18319–18335. https://doi.org/10.1029/92JE01985

Hourdin, F. (2012). *Étude et simulation numérique de la circulation générale des atmosphères planétaires*. (PhD thesis, Doctoral dissertation). Laboratoire de Météorologie Dynamique. Retrieved from https://web.lmd.jussieu.fr/~hourdin/PUBLIS/these.pdf

Hourdin, F., Forget, F., & Talagrand, O. (1995). The sensitivity of the Martian surface pressure and atmospheric mass budget to various parameters: A comparison between numerical simulations and Viking observations. *Journal of Geophysical Research*, *100*(E3), 5501–5523. https://doi.org/10.1029/94JE03079

Hourdin, F., Van, P. L., Forget, F., & Talagrand, O. (1993). Meteorological variability and the annual surface pressure cycle on Mars. *Journal of the Atmospheric Sciences*, *50*(21), 3625–3640. https://doi.org/10.1175/1520-0469(1993)050⟨3625:MVATAS⟩2.0.CO;2

Ingersoll, A. P. (1970). Mars: Occurrence of liquid water. *Science*, *168*(3934), 972–973. https://doi.org/10.1126/science.168.3934.972

Ivanov, A. B., & Muhleman, D. O. (2000). The role of sublimation for the formation of the northern ice cap: Results from the Mars Orbiter Laser Altimeter. *Icarus*, *144*(2), 436–448. https://doi.org/10.1006/icar.1999.6304

James, P. B., Kieffer, H. H., & Paige, D. A. (1992). In M. George (Ed.), *The seasonal cycle of carbon dioxide on Mars* (pp. 934–968).

Joshi, M. M., Lewis, S. R., Read, P. L., & Catling, D. C. (1994). Western boundary currents in the atmosphere of Mars. *Nature*, *367*(6463), 548–551. https://doi.org/10.1038/367548a0

Joshi, M. M., Lewis, S. R., Read, P. L., & Catling, D. C. (1995). Western boundary currents in the Martian atmosphere: Numerical simulations and observational evidence. *Journal of Geophysical Research*, *100*(E3), 5485–5500. https://doi.org/10.1029/94JE02716

Khuller, A. R., & Christensen, P. R. (2021). Evidence of exposed dusty water ice within Martian gullies. *Journal of Geophysical Research: Planets*, *126*(2), e2020JE006539. https://doi.org/10.1029/2020je006539

Khuller, A. R., Christensen, P. R., Harrison, T. N., & Diniega, S. (2021). The distribution of frosts on mars: Links to present-day gully activity. *Journal of Geophysical Research: Planets*, *126*(3), e2020JE006577. https://doi.org/10.1029/2020je006577

Kieffer, H. H. (2013). Thermal model for analysis of Mars infrared mapping. *Journal of Geophysical Research: Planets*, *118*(3), 451–470. https://doi.org/10.1029/2012JE004164

Kreslavsky, M. A., & Head, J. W. (1999). Kilometer-scale slopes on Mars and their correlation with geologic units: Initial results from Mars Orbiter Laser Altimeter (MOLA) data. *Journal of Geophysical Research*, *104*(E9), 21911–21924. https://doi.org/10.1029/1999JE001051

Kreslavsky, M. A., & Head, J. W. (2000). Kilometer-scale roughness of Mars: Results from MOLA data analysis. *Journal of Geophysical Research*, *105*(E11), 26695–26712. https://doi.org/10.1029/2000JE001259

Kreslavsky, M. A., & Head, J. W. (2005). Mars at very low obliquity: Atmospheric collapse and the fate of volatiles. *Geophysical Research Letters*, *32*(12), L12202. https://doi.org/10.1029/2005GL022645

Kreslavsky, M. A., & Head, J. W. (2011). Carbon dioxide glaciers on Mars: Products of recent low obliquity epochs (?). *Icarus*, *216*(1), 111–115. https://doi.org/10.1016/j.icarus.2011.08.020

Lange, L., Forget, F., Dupont, E., Vandemeulebrouck, R., Spiga, A., Millour, E., et al. (2023). Modelling slope microclimates in the Mars Planetary Climate Model [Dataset]. Harvard Dataverse. https://doi.org/10.7910/DVN/NDPNBB

Lange, L., Forget, F., Vincendon, M., Spiga, A., Vos, E., Aharonson, O., et al. (2023). A reappraisal of subtropical subsurface water ice stability on Mars. *Geophysical Research Letters*, *50*, e2023GL105177. https://doi.org/10.1029/2023GL105177

Lange, L., Piqueux, S., & Edwards, C. S. (2022). Gardening of the Martian regolith by diurnal CO_2 frost and the formation of slope streaks. *Journal of Geophysical Research: Planets*, *127*(4), e2021JE006988. https://doi.org/10.1029/2021JE006988

Langevin, Y., Bibring, J. P., Montmessin, F., Forget, F., Vincendon, M., Douté, S., et al. (2007). Observations of the south seasonal cap of Mars during recession in 2004–2006 by the OMEGA visible/near-infrared imaging spectrometer on board Mars Express. *Journal of Geophysical Research*, *112*(E8), E08S12. https://doi.org/10.1029/2006JE002841

Langevin, Y., Poulet, F., Bibring, J.-P., Schmitt, B., Douté, S., & Gondet, B. (2005). Summer evolution of the north polar cap of Mars as observed by OMEGA/Mars express. *Science*, *307*(5715), 1581–1584. https://doi.org/10.1126/science.1109438

Leighton, R. B., & Murray, B. C. (1966). Behavior of carbon dioxide and other volatiles on Mars. *Science*, *153*(3732), 136–144. https://doi.org/10.1126/science.153.3732.136

Litvak, M. L., Mitrofanov, I. G., Kozyrev, A. S., Sanin, A. B., Tretyakov, V. I., Boynton, W. V., et al. (2007). Long-term observations of southern winters on Mars: Estimations of column thickness, mass, and volume density of the seasonal CO2 deposit from HEND/Odyssey data. *Journal of Geophysical Research*, *112*(E3), E03S13. https://doi.org/10.1029/2006je002832

Madeleine, J.-B., Forget, F., Millour, E., Montabone, L., & Wolff, M. J. (2011). Revisiting the radiative impact of dust on Mars using the LMD Global Climate Model. *Journal of Geophysical Research*, *116*(E11), E11010. https://doi.org/10.1029/2011je003855

Madeleine, J.-B., Forget, F., Millour, E., Navarro, T., & Spiga, A. (2012). The influence of radiatively active water ice clouds on the Martian climate. *Geophysical Research Letters*, *39*(23), L23202. https://doi.org/10.1029/2012gl053564

Mahrt, L. (2000). Surface heterogeneity and vertical structure of the boundary layer. *Boundary-Layer Meteorology*, *96*(1), 33–62. https://doi.org/10.1023/A:1002482332477

Malin, M. C., & Edgett, K. S. (2000). Evidence for recent groundwater seepage and surface runoff on Mars. *Science*, *288*(5475), 2330–2335. https://doi.org/10.1126/science.288.5475.2330

Martínez, G. M., Rennó, N., Fischer, E., Borlina, C. S., Hallet, B., Juárez, M. T., et al. (2014). Surface energy budget and thermal inertia at gale crater: Calculations from ground-based measurements. *Journal of Geophysical Research: Planets*, *119*(8), 1822–1838. https://doi.org/10.1002/2014je004618

McEwen, A. S., Dundas, C. M., Mattson, S. S., Toigo, A. D., Ojha, L., Wray, J. J., et al. (2014). Recurring slope lineae in equatorial regions of Mars. *Nature Geoscience*, *7*(1), 53–58. https://doi.org/10.1038/ngeo2014

McEwen, A. S., Ojha, L., Dundas, C. M., Mattson, S. S., Byrne, S., Wray, J. J., et al. (2011). Seasonal flows on warm Martian slopes. *Science*, *333*(6043), 740–743. https://doi.org/10.1126/science.1204816

McKay, C. P. (2009). Snow recurrence sets the depth of dry permafrost at high elevations in the McMurdo Dry Valleys of Antarctica. *Antarctic Science*, *21*(1), 89–94. https://doi.org/10.1017/S0954102008001508

Mellon, M. T., Feldman, W. C., & Prettyman, T. H. (2004). The presence and stability of ground ice in the Southern Hemisphere of Mars. *Icarus*, *169*(2), 324–340. https://doi.org/10.1016/j.icarus.2003.10.022

Mellon, M. T., & Jakosky, B. M. (1993). Geographic variations in the thermal and diffusive stability of ground ice on Mars. *Journal of Geophysical Research*, *98*(E2), 3345–3364. https://doi.org/10.1029/92je02355

Mellon, M. T., & Jakosky, B. M. (1995). The distribution and behavior of Martian ground ice during past and present epochs. *Journal of Geophysical Research*, *100*(E6), 11781–11799. https://doi.org/10.1029/95JE01027

Mellon, M. T., Jakosky, B. M., Kieffer, H. H., & Christensen, P. R. (2000). High-resolution thermal inertia mapping from the Mars global surveyor thermal emission spectrometer. *Icarus*, *148*(2), 437–455. https://doi.org/10.1006/icar.2000.6503

Mellon, M. T., Jakosky, B. M., & Postawko, S. E. (1997). The persistence of equatorial ground ice on Mars. *Journal of Geophysical Research*, *102*(E8), 19357–19369. https://doi.org/10.1029/97je01346

Mellon, M. T., & Phillips, R. J. (2001). Recent gullies on Mars and the source of liquid water. *Journal of Geophysical Research*, *106*(E10), 23165–23179. https://doi.org/10.1029/2000JE001424

Molod, A., Salmun, H., & Waugh, D. W. (2003). A new look at modeling surface heterogeneity: Extending its influence in the vertical. *Journal of Hydrometeorology*, *4*(5), 810–825. https://doi.org/10.1175/1525-7541(2003)004⟨0810:ANLAMS⟩2.0.CO;2

Montabone, L., Forget, F., Millour, E., Wilson, R., Lewis, S., Cantor, B., et al. (2015). Eight-year climatology of dust optical depth on Mars. *Icarus*, *251*, 65–95. https://doi.org/10.1016/j.icarus.2014.12.034

Morgan, G. A., Putzig, N. E., Perry, M. R., Sizemore, H. G., Bramson, A. M., Petersen, E. I., et al. (2021). Availability of subsurface water-ice resources in the northern mid-latitudes of Mars. *Nature Astronomy*, *5*(3), 230–236. https://doi.org/10.1038/s41550-020-01290-z

Murphy, D. M., & Koop, T. (2005). Review of the vapour pressures of ice and supercooled water for atmospheric applications. *Quarterly Journal of the Royal Meteorological Society*, *131*(608), 1539–1565. https://doi.org/10.1256/qj.04.94

Naar, J., Forget, F., Vals, M., Millour, E., Bierjon, A., González-Galindo, F., & Richard, B. (2021). Modeling the global water cycle on Mars with improved physical parametrization. In *European Planetary Science Congress* (p. EPSC2021-559). https://doi.org/10.5194/epsc2021-559

Navarro, T., Madeleine, J.-B., Forget, F., Spiga, A., Millour, E., Montmessin, F., & Määttänen, A. (2014). Global climate modeling of the Martian water cycle with improved microphysics and radiatively active water ice clouds. *Journal of Geophysical Research: Planets*, *119*(7), 1479–1495. https://doi.org/10.1002/2013JE004550

Neumann, G. A., Rowlands, D. D., Lemoine, F. G., Smith, D. E., & Zuber, M. T. (2001). Crossover analysis of Mars orbiter laser altimeter data. *Journal of Geophysical Research*, *106*(E10), 23753–23768. https://doi.org/10.1029/2000je001381

Pál, B., Kereszturi, Á., Forget, F., & Smith, M. D. (2019). Global seasonal variations of the near-surface relative humidity levels on present-day Mars. *Icarus*, *333*, 481–495. https://doi.org/10.1016/j.icarus.2019.07.007

Piqueux, S., Buz, J., Edwards, C. S., Bandfield, J. L., Kleinböhl, A., Kass, D. M., & Hayne, P. O. (2019). Widespread shallow water ice on Mars at high latitudes and midlatitudes. *Geophysical Research Letters*, *46*(24), 14290–14298. https://doi.org/10.1029/2019gl083947

Piqueux, S., Kleinböhl, A., Hayne, P. O., Heavens, N. G., Kass, D. M., McCleese, D. J., et al. (2016). Discovery of a widespread low-latitude diurnal CO_2 frost cycle on Mars. *Journal of Geophysical Research: Planets*, *121*(7), 1174–1189. https://doi.org/10.1002/2016JE005034

Pitman, A. J. (2003). The evolution of, and revolution in, land surface schemes designed for climate models. *International Journal of Climatology*, *23*(5), 479–510. https://doi.org/10.1002/joc.893

Putzig, N. E., & Mellon, M. T. (2007). Apparent thermal inertia and the surface heterogeneity of Mars. *Icarus*, *191*(1), 68–94. https://doi.org/10.1016/j.icarus.2007.05.013

Putzig, N. E., Mellon, M. T., Kretke, K. A., & Arvidson, R. E. (2005). Global thermal inertia and surface properties of Mars from the MGS mapping mission. *Icarus*, *173*(2), 325–341. https://doi.org/10.1016/j.icarus.2004.08.017

Read, P. L., Galperin, B., Larsen, S. E., Lewis, S. R., Määttänen, A., Petrosyan, A., et al. (2017). The Martian planetary boundary layer. In *The atmosphere and climate of Mars* (pp. 172–202). Cambridge University Press. https://doi.org/10.1017/9781139060172.007

Richardson, M. I. (2002). Water ice clouds in the Martian atmosphere: General Circulation Model experiments with a simple cloud scheme. *Journal of Geophysical Research*, *107*(E9), 5064. https://doi.org/10.1029/2001je001804

Russell, P., Thomas, N., Byrne, S., Herkenhoff, K., Fishbaugh, K., Bridges, N., et al. (2008). Seasonally active frost-dust avalanches on a north polar scarp of Mars captured by HiRISE. *Geophysical Research Letters*, *35*(23), L23204. https://doi.org/10.1029/2008gl035790

Saunders, R., Arvidson, R., Badhwar, G., Boynton, W., Christensen, P., Cucinotta, F., et al. (2004). 2001 Mars Odyssey mission summary. *Space Science Reviews*, *110*(1/2), 1–36. https://doi.org/10.1023/b:spac.0000021006.84299.18

Savijärvi, H., & Kauhanen, J. (2008). Surface and boundary-layer modelling for the Mars Exploration Rover sites. *Quarterly Journal of the Royal Meteorological Society*, *134*(632), 635–641. https://doi.org/10.1002/qj.232

Savijärvi, H., & Määttänen, A. (2010). Boundary-layer simulations for the Mars Phoenix lander site. *Quarterly Journal of the Royal Meteorological Society*, *136*(651), 1497–1505. https://doi.org/10.1002/qj.650

Schmidt, F., Andrieu, F., Costard, F., Kocifaj, M., & Meresescu, A. G. (2017). Formation of recurring slope lineae on Mars by rarefied gas-triggered granular flows. *Nature Geoscience*, *10*(4), 270–273. https://doi.org/10.1038/ngeo2917

Schorghofer, N. (2020). Mars: Quantitative evaluation of crocus melting behind boulders. *The Astrophysical Journal*, *890*(1), 49. https://doi.org/10.3847/1538-4357/ab612f

Schorghofer, N. (2022). Planetary-code-collection: User guide of thermal and ice evolution models for planetary surfaces. *Zenodo*. https://doi.org/10.5281/ZENODO.594268

Schorghofer, N., & Aharonson, O. (2005). Stability and exchange of subsurface ice on Mars. *Journal of Geophysical Research*, *110*(E5), E05003. https://doi.org/10.1029/2004JE002350

Schorghofer, N., & Edgett, K. S. (2006). Seasonal surface frost at low latitudes on Mars. *Icarus*, *180*(2), 321–334. https://doi.org/10.1016/j.icarus.2005.08.022

Siegler, M., Aharonson, O., Carey, E., Choukroun, M., Hudson, T., Schorghofer, N., & Xu, S. (2012). Measurements of thermal properties of icy Mars regolith analogs. *Journal of Geophysical Research*, *117*(E3), E03001. https://doi.org/10.1029/2011JE003938

Smith, D., Neumann, G., Ford, P., Arvidson, R., Guinness, E. A., & Slavney, S. (1999). Mars global surveyor laser altimeter precision experiment data record [Dataset]. NASA Planetary Data System. https://pds-geosciences.wustl.edu/citations.html

Smith, D. E., Zuber, M. T., Frey, H. V., Garvin, J. B., Head, J. W., Muhleman, D. O., et al. (2001). Mars Orbiter Laser Altimeter: Experiment summary after the first year of global mapping of Mars. *Journal of Geophysical Research*, *106*(E10), 23689–23722. https://doi.org/10.1029/2000JE001364

Smith, M. D. (2002). The annual cycle of water vapor on Mars as observed by the thermal emission spectrometer. *Journal of Geophysical Research*, *107*(E11), 25-1–25-19. https://doi.org/10.1029/2001JE001522

Smith, M. D. (2004). Interannual variability in TES atmospheric observations of Mars during 1999–2003. *Icarus*, *167*(1), 148–165. https://doi.org/10.1016/j.icarus.2003.09.010

Song, H., Zhang, J., Liu, Y., Sun, Y., & Ni, D. (2023). Modeling the distribution of subsurface seasonal water ice with varying atmospheric conditions at northern low to midlatitudes on Mars. *Icarus*, *389*, 115262. https://doi.org/10.1016/j.icarus.2022.115262

Spiga, A., & Forget, F. (2008). Fast and accurate estimation of solar irradiance on Martian slopes. *Geophysical Research Letters*, *35*(15), L15201. https://doi.org/10.1029/2008gl034956

Spiga, A., Forget, F., Madeleine, J.-B., Montabone, L., Lewis, S. R., & Millour, E. (2011). The impact of Martian mesoscale winds on surface temperature and on the determination of thermal inertia. *Icarus*, *212*(2), 504–519. https://doi.org/10.1016/j.icarus.2011.02.001

Sullivan, R., Thomas, P., Veverka, J., Malin, M., & Edgett, K. (2001). Mass movement slope streaks imaged by the Mars Orbiter Camera. *Journal of Geophysical Research*, *106*(E10), 23607–23633. https://doi.org/10.1029/2000JE001296

Tebolt, M., Levy, J., Goudge, T., & Schorghofer, N. (2020). Slope, elevation, and thermal inertia trends of Martian recurring slope lineae initiation and termination points: Multiple possible processes occurring on coarse, sandy slopes. *Icarus*, *338*, 113536. https://doi.org/10.1016/j.icarus.2019.113536

Tesson, P.-A., Conway, S., Mangold, N., Ciazela, J., Lewis, S., & Mège, D. (2020). Evidence for thermal-stress-induced rockfalls on Mars impact crater slopes. *Icarus*, *342*, 113503. https://doi.org/10.1016/j.icarus.2019.113503

Titus, T. N., Kieffer, H. H., Mullins, K. F., & Christensen, P. R. (2001). TES premapping data: Slab ice and snow flurries in the Martian north polar night. *Journal of Geophysical Research*, *106*(E10), 23181–23196. https://doi.org/10.1029/2000JE001284

Vincendon, M. (2015). Identification of Mars gully activity types associated with ice composition. *Journal of Geophysical Research: Planets*, *120*(11), 1859–1879. https://doi.org/10.1002/2015je004909

Vincendon, M., Forget, F., & Mustard, J. (2010). Water ice at low to midlatitudes on Mars. *Journal of Geophysical Research*, *115*(E10), E10001. https://doi.org/10.1029/2010JE003584

Vincendon, M., Mustard, J., Forget, F., Kreslavsky, M., Spiga, A., Murchie, S., & Bibring, J.-P. (2010). Near-tropical subsurface ice on Mars. *Geophysical Research Letters*, *37*(1). https://doi.org/10.1029/2009gl041426

Wang, F., Cheruy, F., & Dufresne, J.-L. (2016). The improvement of soil thermodynamics and its effects on land surface meteorology in the IPSL climate model. *Geoscientific Model Development*, *9*(1), 363–381. https://doi.org/10.5194/gmd-9-363-2016

Williams, K. E., Dundas, C. M., & Kahre, M. A. (2022). The formation mechanisms for mid-latitude ice scarps on Mars. *Icarus*, *386*, 115174. https://doi.org/10.1016/j.icarus.2022.115174

Williams, K. E., McKay, C. P., & Heldmann, J. (2015). Modeling the effects of Martian surface frost on ice table depth. *Icarus*, *261*, 58–65. https://doi.org/10.1016/j.icarus.2015.08.005

Williams, K. E., Toon, O. B., Heldmann, J. L., McKay, C., & Mellon, M. T. (2008). Stability of mid-latitude snowpacks on Mars. *Icarus*, *196*(2), 565–577. https://doi.org/10.1016/j.icarus.2008.03.017

Wyngaard, J. C. (2004). Toward numerical modeling in the "Terra Incognita". *Journal of the Atmospheric Sciences*, *61*(14), 1816–1826. https://doi.org/10.1175/1520-0469(2004)061⟨1816:TNMITT⟩2.0.CO;2